Eur. Phys. J. C (2015) 75:226
DOI 10.1140/epjc/s10052-015-3422-9

THE EUROPEAN PHYSICAL JOURNAL C

Regular Article - Experimental Physics

Measurement of pion, kaon and proton production in proton–proton collisions at $\sqrt{s} = 7$ TeV

ALICE Collaboration[⋆]

CERN, 1211 Geneva 23, Switzerland

Received: 2 April 2015 / Accepted: 20 April 2015 / Published online: 27 May 2015

Abstract The measurement of primary $\pi^{\pm}$, $K^{\pm}$, p and $\overline{p}$ production at mid-rapidity ($|y| < 0.5$) in proton–proton collisions at $\sqrt{s} = 7$ TeV performed with a large ion collider experiment at the large hadron collider (LHC) is reported. Particle identification is performed using the specific ionisation energy-loss and time-of-flight information, the ring-imaging Cherenkov technique and the kink-topology identification of weak decays of charged kaons. Transverse momentum spectra are measured from 0.1 up to 3 GeV/c for pions, from 0.2 up to 6 GeV/c for kaons and from 0.3 up to 6 GeV/c for protons. The measured spectra and particle ratios are compared with quantum chromodynamics-inspired models, tuned to reproduce also the earlier measurements performed at the LHC. Furthermore, the integrated particle yields and ratios as well as the average transverse momenta are compared with results at lower collision energies.

1 Introduction

The majority of the particles produced at mid-rapidity in proton–proton collisions are low-momentum hadrons not originating from the fragmentation of partons produced in scattering processes with large momentum transfer. Their production, therefore, cannot be computed from first principles via perturbative quantum chromodynamics (pQCD). Currently available models describing hadron-hadron collisions at high energy, such as the event generators PYTHIA6 [1], PYTHIA8 [2,3], EPOS [4,5] and PHOJET [6], combine pQCD calculations for the description of hard processes with phenomenological models for the description of the soft component. The measurement of low-momentum particle production and species composition is therefore important as it provides crucial input for the modelling of the soft component and of the hadronisation processes. Furthermore, it serves as a reference for the same measurement in Pb–Pb collisions to study the properties of the hot and dense strongly interacting medium with partonic degrees of freedom, the quark–gluon plasma, which is created in these collisions. In this paper, the measurement of primary $\pi^{\pm}$, $K^{\pm}$, p and $\overline{p}$ production at mid-rapidity in proton–proton collisions at $\sqrt{s} = 7$ TeV using the ALICE detector [7–10] is presented. Primary particles are defined as prompt particles produced in the collision including decay products, except those from weak decays of light flavour hadrons and muons. Pions, kaons and protons are identified over a wide momentum range by combining the information extracted from the specific ionisation energy loss (dE/dx) measured in the inner tracking system (ITS) [11] and in the time projection chamber (TPC) [12], the time of flight measured in the time-of-flight (TOF) detector [13], the Cherenkov radiation measured in the high-momentum particle identification detector (HMPID) [14] and the kink-topology identification of the weak decays of charged kaons. Similar measurements in proton–proton collisions at $\sqrt{s} = 900$ GeV and 2.76 TeV are reported in [15–17] and are included, together with lower energy data [18–24], in the discussion of the evolution of particle production with collision energy. Similar measurement at the LHC have also been performed in the forward region [25].

The paper is organised as follows. In Sect. 2 the ALICE experimental setup is described, focusing on the detectors and the corresponding particle identification (PID) techniques relevant for the present measurement. Details of the event and track selection criteria and the corrections applied to the measured raw yields are also presented. In Sect. 3 the results on the production of primary $\pi^{\pm}$, $K^{\pm}$, p and $\overline{p}$ are shown. These include the transverse momentum (p_{T}) distributions and the p_{T}-integrated production yields of each particle species and the K/π and p/π ratios. The evolution with collision energy of the p_{T}-integrated particle yields, of their ratios and of their average transverse momenta $\langle p_{\mathrm{T}} \rangle$ is also presented. In Sect. 4 particle spectra and their ratios (K/π and p/π) are compared with models, in particular with different PYTHIA tunes [1–3,26,27], EPOS [4,5] and PHOJET [6]. Section 5 concludes the paper summarizing the results.

⋆ e-mail: alice-publications@cern.ch

2 Experimental setup and data analysis

2.1 The ALICE detector

The ALICE detector was specifically optimised to reconstruct and identify particles over a wide momentum range thanks to the low material budget, the moderate magnetic field and the presence of detectors exploiting all the known PID techniques. A comprehensive description of the ALICE experimental setup and performance can be found in [7–10]. In the following, the PID detectors relevant for the analysis presented in this paper are briefly described, namely ITS, TPC, TOF and HMPID. They are located in the ALICE central barrel in a $B = 0.5$ T solenoidal magnetic field directed along the beam axis. The ITS, TPC and TOF detectors cover the full azimuth (φ) and have a pseudorapidity coverage of $|\eta| < 0.9$, while the HMPID covers the pseudorapidity interval $|\eta| < 0.55$ and the azimuthal angle range $1.2° < \varphi < 58.5°$.

The ITS [11] is the innermost central barrel detector. It is composed of six cylindrical layers of silicon detectors, located at radial distances between 3.9 and 43 cm from the beam axis. The two innermost layers are equipped with silicon pixel detectors (SPD), the two intermediate ones are silicon drift detectors (SDD), while the two outermost ones are silicon strip detectors (SSD). The ITS provides high resolution tracking points close to the beam line, which allows us to reconstruct primary and secondary vertices with high precision, to measure with excellent resolution the distance of closest approach (DCA) of a track to the primary vertex, and to improve the track p_{T} resolution. It is also used as a stand-alone tracker to reconstruct particles that do not reach the TPC or do not cross its sensitive areas. The SDD and SSD are equipped with analogue readout enabling PID via $\mathrm{d}E/\mathrm{d}x$ measurements with a relative resolution of about 10 %.

The TPC [12] is the main tracking detector of the ALICE central barrel. It is a large volume cylindrical chamber with high-granularity readout that surrounds the ITS covering the region $85 < r < 247$ and $-250 < z < +250$ cm in the radial r and longitudinal z directions, respectively. It provides three-dimensional space points and specific ionisation energy loss $\mathrm{d}E/\mathrm{d}x$ with up to 159 samples per track. The relative $\mathrm{d}E/\mathrm{d}x$ resolution is measured to be about 5.5 % for tracks that cross from the centre of the outer edge of the detector.

The TOF detector [13] is a large-area array of multigap resistive plate chambers with an intrinsic time resolution of 50 ps, including the electronic readout contribution. It is a cylindrical detector located at a radial distance $370 < r < 399$ cm from the beam axis. Particles are identified using simultaneously the TOF information with the momentum and track length measured with the ITS and the TPC.

The HMPID [14] is a single-arm proximity-focusing ring imaging Cherenkov (RICH) detector located at 475 cm from the beam axis. The Cherenkov radiator is a 15-mm-thick layer of liquid C_6F_{14} (perfluorohexane) with a refractive index of $n = 1.2989$ at a photon wave length $\lambda = 175$ nm, corresponding to a minimum particle velocity $\beta_{\mathrm{min}} = 0.77$.

In addition to the detectors described above that provide PID information, the VZERO system [28] is used for trigger and event selection. It is composed of two scintillator arrays, which cover the pseudorapidity ranges $2.8 < \eta < 5.1$ and $-3.7 < \eta < -1.7$.

2.2 Data sample, event and track selection

The results presented in this paper are obtained combining five independent analyses, namely ITS stand-alone, TPC–TOF, TOF, HMPID, kink, using different PID methods. The analysed data are proton–proton collisions at $\sqrt{s} = 7$ TeV collected in 2010. During that period, the instantaneous luminosity at the ALICE interaction point was kept within the range $0.6–1.2 \times 10^{29}\ \mathrm{cm}^{-2}\ \mathrm{s}^{-1}$ to limit the collision pile-up probability. Only runs with a collision pile-up probability smaller than 4 % are used in this analysis, leading to an average pile-up rate of 2.5 %. The number of events used in the five independent analyses is reported in Table 1. The data were collected using a minimum-bias trigger, which required a hit in the SPD or in at least one of the VZERO scintillator arrays in coincidence with the arrival of proton bunches from both directions. This trigger selection essentially corresponds to the requirement of having at least one charged particle in 8 units of pseudorapidity. The contamination due to beam-induced background is removed off-line by using the timing information from the VZERO detector, which measures the event time with a resolution of about 1 ns, and the correlation between the number of clusters and track segments (tracklets) in the SPD [15].

Selected events are further required to have a reconstructed primary vertex. For 87 % of the triggered events, the interaction vertex position is determined from the tracks reconstructed in TPC and ITS. For events that do not have a vertex reconstructed from tracks, which are essentially collisions with low multiplicity of charged particles, the primary vertex is reconstructed from the SPD tracklets, which are track segments built from pairs of hits in the two innermost layers of the ITS. Overall, the fraction of events with reconstructed primary vertex, either from tracks or from SPD tracklets, is of 91 %. Accepted events are required to have the reconstructed vertex position along the beam direction, z, within ± 10 cm from the centre of the ALICE central barrel. This ensures good rapidity coverage, uniformity of the particle reconstruction efficiency in ITS and TPC and reduction of the remaining beam-gas contamination. In the following analyses two different sets of tracks are used: the global tracks, reconstructed using information from both ITS and TPC, and the ITS-sa tracks, reconstructed by using

only the hits in the ITS. To limit the contamination due to secondary particles and tracks with wrongly associated hits and to ensure high tracking efficiency, tracks are selected according to the following criteria. The global tracks are required to cross over at least 70 TPC readout rows with a value of $\chi^2/N_{\text{clusters}}$ of the momentum fit in the TPC lower than 4, to have at least two clusters reconstructed in the ITS out of which at least one is in the SPD layers and to have a DCA to the interaction vertex in the longitudinal plane, $\text{DCA}_z < 2$ cm. Furthermore, the daughter tracks of reconstructed kinks are rejected. This last cut is not applied in the kink analysis where a further p_{T}-dependent selection on the DCA of the selected tracks to the primary vertex in the transverse plane (DCA_{xy}) is requested. The global tracks that satisfy these selection criteria have a p_{T} resolution of 1 % at $p_{\text{T}} = 1$ GeV/c and 2 % at $p_{\text{T}} = 10$ GeV/c. The ITS-sa tracks are required to have at least four ITS clusters out of which at least one in the SPD layers and three in the SSD and SDD, $\chi^2/N_{\text{clusters}} < 2.5$ and a DCA_{xy} satisfying a p_{T}-dependent upper cut corresponding to 7 times the DCA resolution. The selected ITS-sa tracks have a maximum p_{T} resolution of 6 % for pions, 8 % for kaons and 10 % for protons in the p_{T} range used in the analysis. Global and ITS-sa tracks have a similar resolution in the DCA_{xy} parameter, that is, 75 μm at $p_{\text{T}} = 1$ GeV/c and 20 μm at $p_{\text{T}} = 15$ GeV/c [29], which is well reproduced in the simulation of the detector performance. The final spectra are calculated for $|y| < 0.5$.

2.3 Particle identification strategy

To measure the production of $\pi^{\pm}$, $K^{\pm}$, p and $\overline{p}$ over a wide p_{T} range, results from five independent analyses, namely ITS-sa, TPC–TOF, TOF, HMPID and kink, are combined. Each analysis uses different PID signals in order to identify particles in the complementary p_{T} ranges reported in Table 1. In the following, the PID strategies used by ITS-sa, TPC–TOF and TOF analyses are briefly summarised since they are already discussed in detail in [15,30], while the HMPID analysis, presented here for the first time, and the kink analysis, modified with respect to that described in [15], are presented in more detail.

2.3.1 ITS stand-alone analysis

In this analysis ITS-sa tracks are used and particles are identified by comparing the $\text{d}E/\text{d}x$ measurement provided by the ITS detector with the expected values at a given momentum p under the corresponding mass hypotheses. In Fig. 1, the measured $\text{d}E/\text{d}x$ values are shown as a function of track momentum together with the curves of the energy loss for the different particle species, which are calculated using the PHOBOS parametrisation [31] of the Bethe–Bloch curves at large $\beta\gamma$ and with a polynomial to correct for instrumental effects. A single identity is assigned to each track according to the mass hypothesis for which the expected specific energy-loss value is the closest to the measured $\text{d}E/\text{d}x$ for a track with momentum p. No explicit selection on the difference between the measured and expected values is applied except for a lower limit on pions set to two times the $\text{d}E/\text{d}x$ resolution (σ) and an upper limit on protons given by the mid-point between the proton and the deuteron expected $\text{d}E/\text{d}x$. The ITS $\text{d}E/\text{d}x$ is calculated as a truncated mean of three or four $\text{d}E/\text{d}x$ values provided by the SDD and SSD layers. The truncated mean is the average of the lowest two $\text{d}E/\text{d}x$ values in case signals in all the four layers are available, or as a weighted average of the lowest (weight 1) and the second lowest (weight 1/2) values in the case where only three $\text{d}E/\text{d}x$ sam-

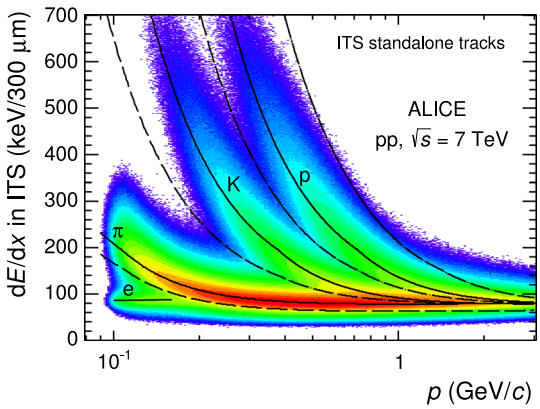

Fig. 1 Distribution of $\text{d}E/\text{d}x$ as a function of momentum (p) measured in the ITS using ITS-sa tracks in $|\eta| < 0.9$. The *continuous curves* represent the parametrisation of $\text{d}E/\text{d}x$ for e, π, K and p while the *dashed curves* are the bands used in the PID procedure

Table 1 Number of analysed events and p_{T} range (GeV/c) covered by each analysis

Analysis	# of events	π	K	p
ITS-sa	5.4×10^7	0.1–0.6	0.2–0.5	0.3–0.6
TPC–TOF	5.4×10^7	0.25–1.2	0.3–1.2	0.45–2.0
TOF	5.4×10^7	0.5–2.5	0.5–2.4	0.8–4.0
HMPID	8.1×10^7	1.5–3.0	1.5–3.0	1.5–6.0
Kink	16.9×10^7	–	0.2–6.0	–

ples are measured. Even with this truncated mean approach, used to reduce the effect of the tail of the Landau distribution at large dE/dx, the small number of samples results in residual non-Gaussian tails in the dE/dx distribution, which are partially reproduced in simulation. These non-Gaussian tails increase the misidentification rate, e.g. pions falling in the kaon identification bands. The misidentification probability is estimated using a Monte-Carlo simulations where the particle abundances were adjusted to those observed in data. This correction is at most 10 % in the p_{T} range of this analysis. In order to check possible systematic effects due to these non-Gaussian tails and their imperfect description in Monte-Carlo simulations, the analysis was repeated with different strategies for the particle identification, namely using a 3σ compatibility band around the expected dE/dx curves and extracting the yields of pions, kaons and protons using the unfolding method described in [15], which is based on fits to the dE/dx distributions in each p_{T} interval. The difference among the results from these different analysis strategies is assigned as a systematic uncertainty due to the PID.

2.3.2 TPC–TOF analysis

In this analysis global tracks are used and particle identification is performed by comparing the measured PID signals in the TPC and TOF detectors (dE/dx, time of flight) with the expected values for different mass hypotheses. An identity is assigned to a track if the measured signal differs from the expected value by less than three times its resolution σ. For pions and protons with $p_{\mathrm{T}} < 0.6$ GeV/c and kaons with $p_{\mathrm{T}} < 0.5$ GeV/c, a compatibility within 3σ is required on the dE/dx measurement provided by the TPC computed as a truncated mean of the lowest 60 % of the available dE/dx samples. The dE/dx resulting from this truncated mean approach is Gaussian and it is shown in Fig. 2 as a function of the track momentum together with the expected energy-loss curves (see [32] for a discussion of the dE/dx parametrisation).

Above these p_{T} thresholds, i.e. $p_{\mathrm{T}} \geq 0.6$ GeV/c for pions and protons and $p_{\mathrm{T}} \geq 0.5$ GeV/c for kaons, a three σ requirement is applied to both the dE/dx measurement provided by the TPC and the time of flight t_{tof} provided by the TOF detector. The time of flight t_{tof}, as will be described in more detail in the next section, is the difference between the arrival time τ_{TOF} measured with the TOF detector and the event start time t_0, namely $t_{\mathrm{tof}} = \tau_{\mathrm{TOF}} - t_0$. The additional condition on the TOF signal helps in extending the particle identification on a track-by-track basis to higher p_{T} where the TPC separation power decreases. The particles for which the TOF signal is available are a sub-sample of the global tracks reconstructed using ITS and TPC information. The TOF information is not available for tracks that cross inactive regions of the TOF

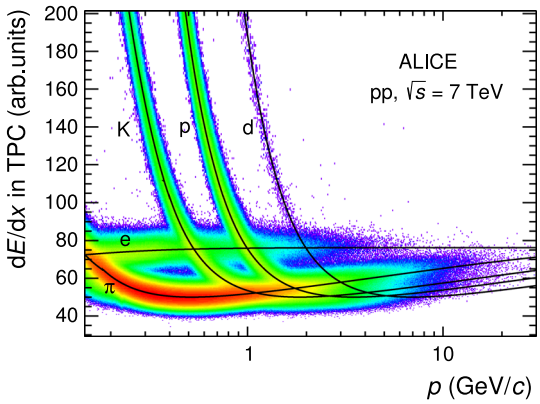

Fig. 2 Distribution of dE/dx as a function of momentum (p) measured in the TPC using global tracks for $|\eta| < 0.9$. The *continuous curves* represent the Bethe–Bloch parametrisation

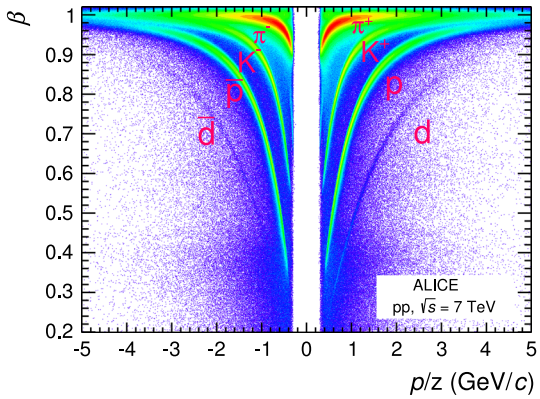

Fig. 3 Particle velocity β measured by the TOF detector as a function of the rigidity p/z, where z is the particle charge, for $|\eta| < 0.9$

detector, for particles that decay or interact with the material before the TOF and for tracks whose trajectory, after prolongation from the TPC outer radius, is not matched with a hit in the TOF detector. The fraction of global tracks with associated TOF information (TOF matching efficiency) depends on the particle species and p_{T} as well as on the fraction of the TOF active readout channels. For the data analysis presented in this paper the matching efficiency increases with increasing p_{T} until it saturates, e.g. at about 65 % for pions with $p_{\mathrm{T}} > 1$ GeV/c. In Fig. 3 the velocity β of the tracks, computed from the trajectory length measured with the ITS and TPC and the time of flight measured with the TOF, is reported as a function of the rigidity p/z, where z is the charge assigned based on the measured direction of the track curvature.

More than one identity can be assigned to a track if it fulfils PID and rapidity selection criteria for different particle species. The frequency of such cases is at most 0.5 % in the momentum range used in this analysis. The misidentification of primary particles is computed and corrected for using Monte-Carlo simulations. It is at most 2 % for pions and protons and 8 % for kaons in the considered p_{T} ranges. The

correction of the raw spectra for the misidentified particles provides also a way to remove the overestimation of the total number of particles introduced by the possibility, described above, to assign more than one identity to a track.

2.3.3 TOF analysis

This analysis uses the sub-sample of global tracks for which a TOF measurement is available. The PID procedure utilises a statistical unfolding approach that provides a p_{T} reach higher than the three σ approach described in the previous section. The procedure is based on the comparison between the measured time of flight from the primary vertex to the TOF detector, t_{tof}, and the time expected under a given mass hypothesis, t_i^{exp} ($i = \pi, K, p$), namely on the variable $\Delta t_i = t_{\mathrm{tof}} - t_i^{\mathrm{exp}}$. As mentioned in the previous section, the time of flight t_{tof} is defined as the difference between the time measured with the TOF detector τ_{TOF} and the event start time t_0. The t_0 value is computed from the analysed tracks themselves on an event-by-event basis, using a combinatorial algorithm which compares the measured τ_{TOF} with the expected ones for different mass hypotheses. The track under study is excluded to avoid any bias in the PID procedure [13,15]. In case the TOF t_0 algorithm fails, the average beam-beam interaction time is used. The former approach provides a better t_0 resolution, but it requires at least three reconstructed tracks with an associated TOF timing measurement. The yield of particles of species i in a given p_{T} interval is obtained by fitting the distribution of the variable Δt_i obtained from all the tracks regardless of the method used to compute the t_0. This distribution is composed of the signal from particles of species i, which is centred at $\Delta t_i = 0$, and two distinct populations corresponding to the other two hadron species, $j, k \neq i$. The Δt_i distribution is therefore fitted with the sum of three functions $f(\Delta t_i)$, one for the signal and two for the other hadron species, as shown in Fig. 4. The $f(\Delta t_i)$ functional forms are defined using the data in the region of clear species separation. The TOF signal is not purely Gaussian and it is described by a function $f(\Delta t_i)$ that is composed of a Gaussian term and an exponential tail at high Δt_i mainly due to tracks inducing signals in more than one elementary detector readout element [13]. The raw yield of the species i is given by the integral of the signal fit function.

The reach in p_{T} of this PID method depends on the resolution of Δt_i, that is, the combination of the TOF detector intrinsic resolution, the uncertainty on the start time and the tracking and momentum resolution. Its value, for the data used in this analysis, is about 120 ps leading to 2σ pion–kaon and kaon–proton separation at $p_{\mathrm{T}} = 2.5$ GeV/c and $p_{\mathrm{T}} = 4.0$ GeV/c, respectively. This PID procedure has the advantage of not requiring a Monte-Carlo-based correction for misidentification because the contamination under the signal of particles of species i due to other particle species is accounted for by the background fit functions.

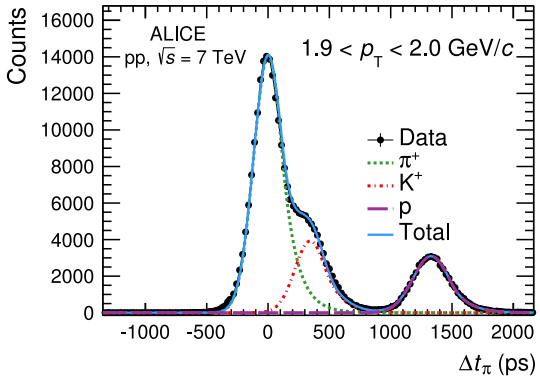

Fig. 4 Distribution of Δt_i assuming the pion mass hypothesis in the transverse momentum interval $1.9 < p_{\mathrm{T}} < 2.0$ GeV/c. The data (*black points*) are fitted with a function (*light blue line*) that is the sum of the signal due to pions (*green dotted line*) and the two populations corresponding to kaons (*red dotted line*) and protons (*purple dashed line*)

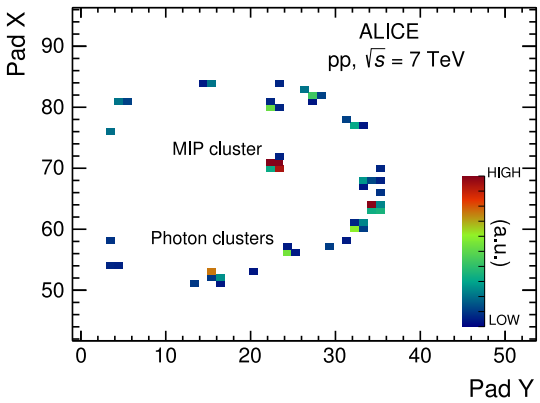

Fig. 5 Display of a Cherenkov ring detected in a module of HMPID for an inclined track crossing the detector. The *colours* are proportional to the pad charge signal

2.3.4 HMPID analysis

The HMPID is a RICH detector in a proximity focusing layout in which the primary ionizing charged particle generates Cherenkov light inside a liquid C_6F_{14} radiator [14]. The UV photons are converted into photoelectrons in a thin CsI film of the PhotoCathodes (PCs) and the photoelectrons are amplified in an avalanche process inside a multi-wire proportional chamber operated with CH_4. To obtain the position sensitivity for the reconstruction of the Cherenkov rings, the PCs are segmented into pads. The final image of a Cherenkov ring is then formed by a cluster of pads (called a "MIP" cluster) associated to the primary ionisation of the particle and the photoelectron clusters associated to Cherenkov photons. In Fig. 5 a typical Cherenkov ring is shown.

In this analysis, the sub-sample of global tracks that reach the HMPID detector and produce the Cherenkov rings is used. Starting from the photoelectron cluster coordinates on the photocathode, a back-tracking algorithm calculates the corresponding single photon Cherenkov angle by using the impact angle of a track extrapolated from the central tracking detectors up to the radiator volume. A selection on the distance ($d_{\mathrm{MIP-trk}}$) computed on the cathode plane between the centroid of the MIP cluster and the track extrapolation, set to $d_{\mathrm{MIP-trk}} < 5$ cm, rejects fake associations in the detector. Background discrimination is performed using the Hough transform method (HTM) [33]. The mean Cherenkov angle $\langle\theta_{\mathrm{ckov}}\rangle$ is obtained if at least three photoelectron clusters are detected.

For a given track, $\langle\theta_{\mathrm{ckov}}\rangle$ is computed as the weighted average of the single photon angles (if any) selected by HTM. Pions, kaons and protons become indistinguishable at high momentum when the resolution on $\langle\theta_{\mathrm{ckov}}\rangle$ reaches 3.5 mrad. The angle $\langle\theta_{\mathrm{ckov}}\rangle$ as a function of the track momentum is shown in Fig. 6, where the solid lines represent the θ_{ckov} dependence on the particle momentum

$$\theta_{\mathrm{ckov}} = \cos^{-1}\frac{\sqrt{p^2+m^2}}{np}, \tag{1}$$

where n is the refractive index of the liquid radiator, m the mass of the particle and p its momentum.

This analysis is performed for $p > 1.5$ GeV/c, where pions, kaons and protons produce a ring with enough photoelectron clusters to be reconstructed. If the track momentum is below the threshold to produce Cherenkov photons, background clusters could be wrongly associated to the track. As an example the few entries visible in Fig. 6 between the pion and kaon bands at low $\langle\theta_{\mathrm{ckov}}\rangle$ correspond to wrong associations of clusters with a kaon or a proton below the threshold to produce Cherenkov photons.

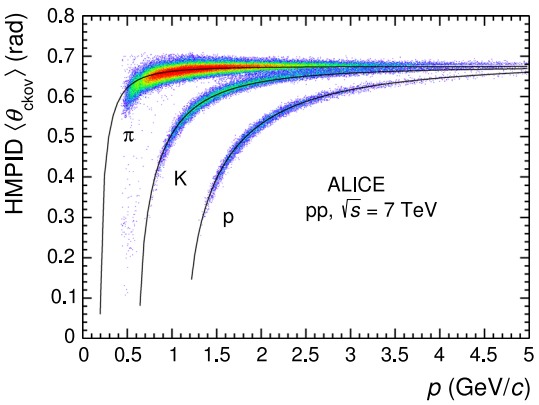

Fig. 6 Mean Cherenkov angle $\langle\theta_{\mathrm{ckov}}\rangle$ measured with HMPID in its full geometrical acceptance as a function of the particle momentum p for positively and negatively charged tracks. The *solid lines* represent the theoretical curves for each particle species

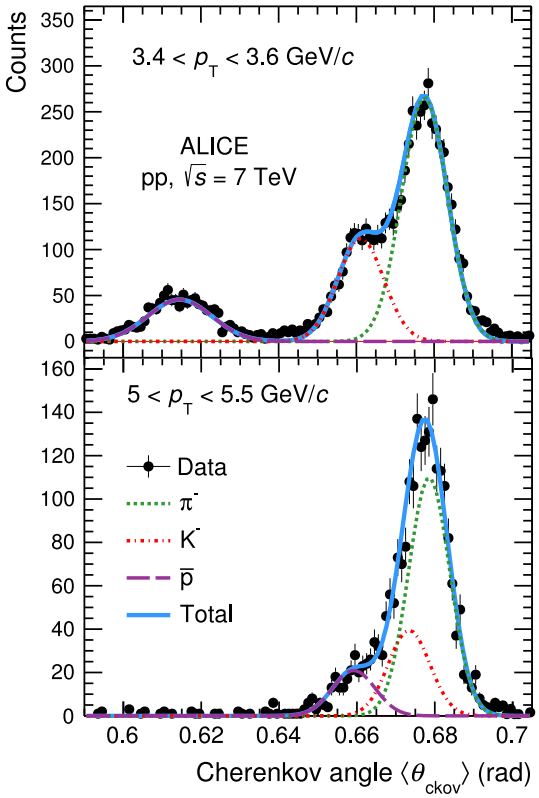

Fig. 7 Distributions of $\langle\theta_{\mathrm{ckov}}\rangle$ measured with the HMPID in the two narrow p_{T} intervals $3.4 < p_{\mathrm{T}} < 3.6$ GeV/c (*top*) and $5 < p_{\mathrm{T}} < 5.5$ GeV/c (*bottom*) for tracks from negatively charged particles. *Solid lines* represent the total fit (sum of three Gaussian functions). *Dotted lines* correspond to pion, kaon and proton signals. The *background* is negligible

The particle yields are extracted from a fit to the Cherenkov angle distribution in narrow transverse momentum intervals. In Fig. 7, examples of the reconstructed Cherenkov angle distributions in two narrow p_{T} intervals ($3.4 < p_{\mathrm{T}} < 3.6$ GeV/c and $5 < p_{\mathrm{T}} < 5.5$ GeV/c) for negatively charged tracks are shown.

The background, mainly due to noisy pads and photoelectron clusters from other rings overlapping to the reconstructed one, is negligible in the momentum range considered in this analysis. The fit function (shown as a solid line in Fig. 7) is a sum of three Gaussian functions, one for each particle species (dashed lines), whose mean and sigma are fixed to the Monte-Carlo values.

The extracted separation power of hadron identification in the HMPID as a function of p_{T} is shown in Fig. 8. The separation between pions and kaons (kaons and protons) is expressed as the difference between the means of the $\langle\theta_{\mathrm{ckov}}\rangle$ angle Gaussian distributions for the two given particle species ($\Delta_{\pi,\mathrm{K}}$ or $\Delta_{K,p}$) divided by the average of the Gaussian widths of the two distributions, i.e. $(\sigma_\pi + \sigma_K)/2$ or $(\sigma_K + \sigma_p)/2$. A separation at 3σ level in $\langle\theta_{\mathrm{ckov}}\rangle$ is achieved up to $p_{\mathrm{T}} = 3$ GeV/c for K–π and up to $p_{\mathrm{T}} = 5$ GeV/c for K–p.

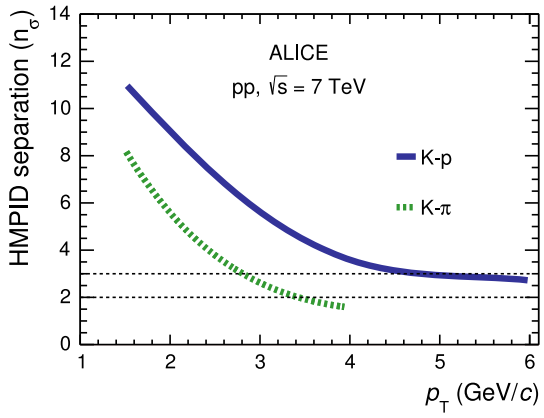

Fig. 8 Separation power (n_σ) of hadron identification in the HMPID as a function of p_T. The separation n_σ of pions and kaons (kaons and protons) is defined as the difference between the average of the Gaussian distributions of $\langle\theta_{ckov}\rangle$ for the two hadron species divided by the average of the Gaussian widths of the two distributions

The separation at 6 GeV/c for $K-p$ can be extrapolated from the curve and it is about 2.5σ.

The HMPID geometrical acceptance is about 5 % for tracks with high momentum. Therefore the analysis of HMPID required one to analyse a larger data sample with respect to the other PID methods, as reported in Table 1. The total efficiency is the convolution of the tracking, matching and PID efficiencies. The PID efficiency of this method is determined by the Cherenkov angle reconstruction efficiency. It has been computed by means of Monte-Carlo simulations and it reaches 90 % for particles with velocity $\beta \sim 1$. As a cross check, the PID efficiency has been determined using clean samples of protons and pions from Λ and K^0_s decays. The measured efficiency agrees within the statistical uncertainties with the Monte-Carlo estimates, in the momentum range $1.5 < p_T < 6$ GeV/c. Moreover, the correction due to the $d_{MIP-trk}$ cut is computed from the same sample of identified protons and pions from Λ and K^0_s decays.

2.3.5 Kink analysis

Charged kaons can also be identified in the TPC by reconstructing their weak-decay vertices, which exhibit a characteristic kink topology defined by a decay vertex with two tracks (mother and daughter) having the same charge. This procedure extends the measurement of charged kaons on a track-by-track basis to $p_T = 6$ GeV/c. The algorithm for the kink reconstruction is applied inside a fiducial volume of the TPC, namely $130 < R < 200$ cm, needed to reconstruct both the mother and the daughter tracks. The mother track is selected with similar criteria to the global tracks (Sect. 2.2), but with a looser selection on the minimum number of TPC clusters, which is set to 20, and a wider rapidity range

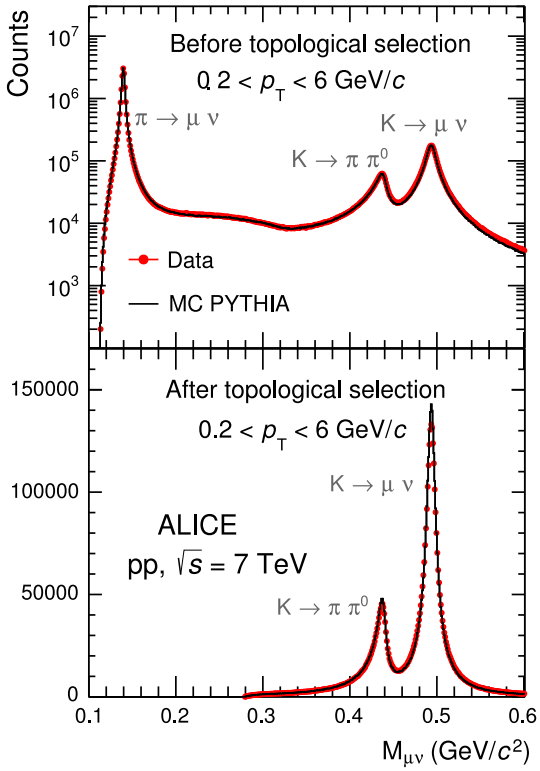

Fig. 9 Kink invariant mass $M_{\mu\nu}$ in data (*red circles*) and Monte-Carlo (*black line*) for summed particles and antiparticles, integrated over the mother transverse momentum range $0.2 < p_T < 6.0$ GeV/c and $|y| < 0.7$ before (*top panel*) and after (*bottom panel*) the topological selections, based mainly on the q_T and the maximum decay opening angle

set to $|y| < 0.7$ to increase the statistics of kink candidates. No selections are applied on the charged daughter track. The reconstructed invariant mass $M_{\mu\nu}$ is calculated assuming the charged daughter track to be a muon and the undetected neutral daughter track to be a neutrino. The neutrino momentum is the difference between the measured momenta of the mother particle and of the charged daughter.

The $M_{\mu\nu}$ distribution, for summed positive and negative charges, integrated over the mother transverse momentum range $0.2 < p_T < 6.0$ GeV/c is reported in the top panel of Fig. 9 for both data and PYTHIA simulations normalised to the same number of entries. Three peaks are present: one centred on the kaon mass due to the kaon decays $K \rightarrow \mu + \nu_\mu$ (branching ratio BR = 63.55 %), one centred at $M_{\mu\nu} = 0.43$ GeV/c^2 due to the $K \rightarrow \pi + \pi^0$ decay (BR = 20.66 %), whose kinematics is calculated with wrong mass assumptions, and the peak due to pion decays $\pi \rightarrow \mu + \nu_\mu$ (BR = 99.99 %). The width of the peaks reflects the momentum resolution of the detector, which is well reproduced in Monte-Carlo simulations. The two-body kinematics of the kink topology allows one to separate kaon decays from the main source of background due to charged pion decays [15]. In the $\mu + \nu_\mu$ channel, the upper limit of the q_T vari-

able, where q_{T} is defined as the transverse momentum of the daughter track with respect to the mother's direction, is 236 MeV/c for muons from kaon decays and 30 MeV/c for muons from pion decays. To remove most of the pion decays, a $q_{\mathrm{T}} > 120$ MeV/c selection is applied. The background is further reduced by rejecting kink decays for which the decay angle, namely the angle between the momenta of the mother and the charged daughter tracks is larger than the maximum angle allowed under the hypothesis $K \rightarrow \mu + \nu_{\mu}$. The bottom panel of Fig. 9 shows the invariant mass distribution of the kaon candidates with mother transverse momentum $0.2 < p_{\mathrm{T}} < 6.0$ GeV/c after the topological selection criteria for kaon identification (mainly the q_{T} and decay angle cuts) are applied. It is evident that only the two peaks coming from kaon decays are present, while the pion background peak is removed. The broad structure on the left originates from the three-body decays of kaons. The agreement between data and simulations in this figure (Fig. 9) is better than 8 %. Most of the selected mother tracks have a dE/dx in the TPC which is compatible with the values expected for kaons. Tracks outside 3.5σ from the expected kaon dE/dx have been removed to attain a purity >97 % in the p_{T} range studied in this analysis. These rejected tracks are <4 %, have $p_{\mathrm{T}} < 0.8$ GeV/c and are, according to Monte-Carlo studies, pions. The raw kaon spectra are obtained from the integral of the invariant mass distribution computed in narrow p_{T} intervals after the topological selection criteria on the q_{T}, the decay opening angle and the compatibility with the expected dE/dx for kaons are applied. The kaon misidentification is computed and corrected for by using Monte-Carlo simulations. It depends on the mother's transverse momentum with a maximum value of 3.6 % at 0.8 GeV/c and a minimum of 2 % at 1 GeV/c, remaining almost flat up to $p_{\mathrm{T}} = 6$ GeV/c. Its average value in the p_{T} range considered in this analysis is 2.1 %.

2.4 Correction of raw spectra

To obtain the p_{T} distributions of primary π, K and p, the contribution of secondaries is subtracted from the raw spectra. Then the spectra are corrected for the PID efficiency, the misidentification probability, the acceptance, the reconstruction and the selection efficiencies according to

$$\frac{\mathrm{d}^2N}{\mathrm{d}p_{\mathrm{T}}\mathrm{d}y} = N_{\mathrm{raw}}(p_{\mathrm{T}})\frac{1}{\Delta p_{\mathrm{T}}\Delta y}\frac{1-s(p_{\mathrm{T}})}{\varepsilon(p_{\mathrm{T}})}\cdot f(p_{\mathrm{T}}), \qquad (2)$$

where $N_{\mathrm{raw}}(p_{\mathrm{T}})\frac{1}{\Delta p_{\mathrm{T}}\Delta y}$ is the raw yield in a given p_{T} interval, $s(p_{\mathrm{T}})$ is the total contamination including effects of secondary and misidentified particles, $\varepsilon(p_{\mathrm{T}})$ is the acceptance $\times$ efficiency including PID efficiency, detector acceptance, reconstruction and selection efficiencies and $f(p_{\mathrm{T}})$ is an additional factor to correct for imperfections of the cross sections for antiparticle interactions with the material used in the GEANT3 code.

The contamination due to weak decays of light flavour hadrons (mainly K^0_s affecting π spectra and Λ and Σ^+ affecting p spectra) and interactions with the material has to be computed and subtracted from the raw spectra. Since strangeness production is underestimated in the event generators and the interactions of low p_{T} particles with the material are not properly modelled in the transport codes, the secondary-particle contribution is evaluated with a data-driven approach. This approach exploits the high resolution determination of the track impact parameter in the transverse plane, DCA$_{xy}$, and the fact that secondary particles from strange hadron decays and interactions with the detector material, originate from secondary vertices significantly displaced from the interaction point and, therefore, their tracks have, on average, larger absolute values of DCA$_{xy}$ with respect to primary particles. Hence, for each of the PID techniques described in the previous sections, the contribution of secondary particles to the measured raw yield of a given hadron species in a given p_{T} interval is extracted by fitting the measured distributions of DCA$_{xy}$ of the tracks identified as particles of the considered hadron species. The DCA$_{xy}$ distributions are modelled with three contributions, called templates. Their shapes are extracted for each p_{T} interval and particle species from simulations, as described in [30], and represent the DCA$_{xy}$ distributions of primary particles, secondary particles from weak decays of strange hadrons and secondary particles produced in the interactions with the detector material, respectively. An example for protons in the interval $0.55 < p_{\mathrm{T}} < 0.60$ GeV/c is shown in Fig. 10.

The correction for secondary-particle contamination is relevant for $\pi^{\pm}$ (from 10 % at low p_{T} to <2 % at high p_{T}),

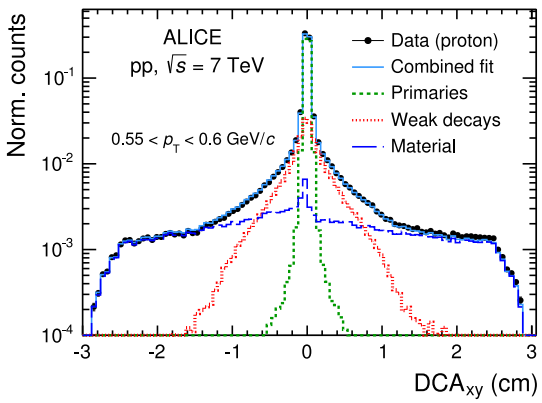

Fig. 10 Proton DCA$_{xy}$ distribution in the range $0.55 < p_{\mathrm{T}} < 0.60$ GeV/c together with the Monte-Carlo templates for primary protons (*green dotted line*), secondary protons from weak decays (*red dotted line*) and secondary protons produced in interactions with the detector material (*blue dashed line*) which are fitted to the data. The *light blue line* represents the combined fit, while the *black dots* are the data

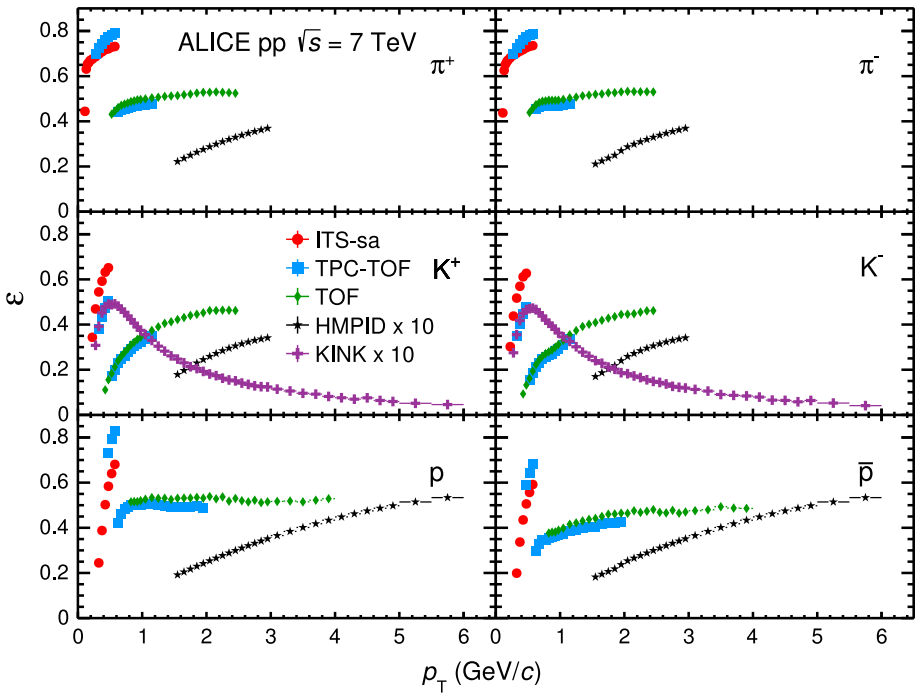

Fig. 11 Correction factors [$\varepsilon(p_{\mathrm{T}})$ in Eq. 2] for π^+, K^+ and p (*left panel*) and their antiparticles (*right panel*) accounting for PID efficiency, detector acceptance, reconstruction and selection efficiencies for ITS-sa (*red circles*), TPC–TOF (*light blue squares*), TOF (*green diamonds*), HMPID (*black stars*) and kink (*purple crosses*) analyses

p and $\overline{p}$ (from 35 % at low p_{T} to 2 % at high p_{T}). Due to the different track and PID selections the contribution of secondaries is different for each analysis.

In the case of kaons, the contamination from secondary particles is negligible, except for the TPC–TOF analysis where a contamination originating from secondary $\mathrm{e}^{\pm}$ produced by photon conversions in the detector material is present. This contamination is significant only in the momentum range $0.4 < p < 0.6$ GeV/c, where the dE/dx of kaons and electrons in the TPC gas are similar, not allowing for their separation, as shown in Fig. 2. Therefore, in the case of kaons, the fit to the DCA_{xy} distributions is used only in the TPC–TOF analysis for $p_{\mathrm{T}} < 0.5$ GeV/c to subtract the contamination due to secondary $\mathrm{e}^{\pm}$. This contamination is about 16 % for $p_{\mathrm{T}} = 0.5$ GeV/c.

The resulting spectra are corrected for the detector acceptance and for the reconstruction and selection efficiencies. This correction is specific to each analysis and accounts for the acceptance of the detector used in the PID procedure, the trigger selection and the vertex and track reconstruction efficiencies. They are evaluated by performing the same analyses on simulated events generated with PYTHIA 6.4 (Perugia0 tune) [26]. The particles are propagated through the detector using the GEANT3 transport code [34], where the detector geometry and response as well as the data taking conditions are reproduced in detail.

In Fig. 11 the efficiency $\varepsilon(p_{\mathrm{T}})$, specific to each analysis, accounting for PID efficiency, acceptance, reconstruction and selection efficiencies are shown. The lower value of ε for HMPID and kink analyses is due to the limited geometrical acceptance of the HMPID detector and to the limited TPC fiducial volume used for the kink vertex reconstruction. The drop in the correction for the TPC–TOF analysis at $p_{\mathrm{T}} = 0.6$ GeV/c for pions and protons and $p_{\mathrm{T}} = 0.5$ GeV/c for kaons is due to the efficiency of track propagation to the TOF. The ITS-sa analysis has a larger kaon efficiency than the TPC–TOF analysis at low p_{T} because the ITS-sa tracking allows the reconstruction of kaons that decay before reaching the TPC. The corrections for particles (left panel of Fig. 11) and antiparticles (right panel) are compatible within the uncertainties.

Since GEANT3 does not describe well the interaction of low-momentum $\overline{p}$ and K^- with the material, corrections to the efficiencies, estimated with a dedicated FLUKA simulation [30,35], are applied. The correction factor $f(p_{\mathrm{T}})$ is $0.71 < f(p_{\mathrm{T}}) < 1$ for $\overline{p}$ and $0.95 < f(p_{\mathrm{T}}) < 1$ for K^-.

The corrected spectra are, finally, normalised to the number of inelastic proton–proton collisions that is obtained from the number of analysed minimum-bias events via the scaling factor 0.852 as described in [36].

2.5 Systematic uncertainties

The main sources of systematic uncertainties, for each analysis, are summarised in Table 2. They are related to the PID procedure, the subtraction of the contribution from secondary particles, imperfect description of the material budget in the Monte-Carlo simulation, particle interactions in the detector material, tracking efficiency and variables used for the track selection.

Table 2 Sources of systematic uncertainties on the corrected spectra $\frac{d^2N}{dp_T dy}$. In case of p_T-dependent systematic uncertainty, the values in the lowest and highest p_T intervals are reported

	$\pi^{\pm}$ (%)	$K^{\pm}$ (%)	p and $\overline{p}$ (%)
Source of uncertainty common to all the analyses			
Correction for secondaries	<1		5–1.5 (p)
			1.5 ($\overline{p}$)
Material budget	5–Negl.	3–Negl.	3–Negl.
Cross sections for interactions in the material	2–1	4–1	4–Negl. (p)
			6–1 ($\overline{p}$)
ITS–TPC matching (excluded in ITS-sa analysis)	3	3	3
Source of uncertainty specific to an analysis			
ITS-sa PID	2	4	4.5
Tracking efficiency (ITS-sa tracks)	3	3	3
$E \times B$ effect	3	3	3
TPC–TOF PID	<1	1–5	<1
Tracking efficiency (global tracks)	2	2	2
Matching efficiency	3	6	4
($p_T > 0.5$ GeV/c for K and 0.6 GeV/c for π, p)			
TOF PID	0.5–3	1–11	1–14
Tracking efficiency (global tracks)	2	2	2
Matching efficiency	3	6	4
HMPID PID	4	5	5–9
Tracking efficiency (global tracks)	5	5	7
$d_{MIP-trk}$ cut	2–6	2–6	2–6
Kink PID		3	
Tracking efficiency (global tracks)		2	
Kink reconstruction efficiency		3	
Kink contamination		3.6–2	

The systematic uncertainties introduced by the PID procedure are estimated differently depending on the specific analysis. In the ITS-sa analysis different techniques are used for the identification: a 3σ compatibility cut and an unfolding method as described in Sect. 2.3.1. In the TPC–TOF analysis the 3σ selection is varied to 2σ and 4σ. Furthermore, the systematic uncertainty on the estimated contamination from misidentified hadrons, which is due to the different relative abundances of pions, kaons and protons in data and simulation, has been estimated to be below 1 % for pions and protons and below 4 % for kaons. In TOF and HMPID analyses the parameters of the fit function used to extract the raw yields are varied (one at a time) by ± 10 %.

The systematic uncertainty due to the subtraction of secondary particles is estimated by changing the fit range of the DCA_{xy} distribution. The shape of the DCA_{xy} template for p and $\overline{p}$ from weak decays is also varied by modifying the relative contribution of the different mother particles. The main sources of p and $\overline{p}$ from weak decays are Λ and Σ^+ (and their antiparticles), which have significantly different mean proper decay lengths ($c\tau = 7.89$ and 2.404 cm, respectively [37]). Therefore, the DCA template of protons from weak decays depends on the Λ to Σ^+ ratio in the event generator used in the simulation.

To evaluate the systematic effect due to the uncertainty in the material budget (about ± 7 % [38]), the efficiency corrections are computed by using Monte-Carlo simulations with the material budget modified by this percentage. The systematic uncertainties in modelling the particle interactions with the detector material are evaluated using different transport codes, as described in [30].

For all the analyses, the systematic uncertainties related to tracking procedure are estimated by varying the track selection criteria (e.g. number of crossed readout rows in TPC, number of clusters in ITS, DCA_z, DCA_{xy}) reported in Sect. 2.2. For global tracks an additional uncertainty, related to the ITS–TPC matching, is also included. It is estimated by comparing the matching efficiency in data and Monte-Carlo simulations.

Further systematic uncertainty sources, specific to each analysis, are also evaluated. In the case of the ITS-sa analysis, the Lorentz force causes shifts of the cluster position in

the ITS, pushing the charge in opposite directions depending on the polarity of the magnetic field of the experiment ($E \times B$ effect). This effect is not fully reproduced in the simulation. It is estimated by analysing data samples collected with different magnetic field polarities, which resulted in an uncertainty of 3 %. In the case of TPC–TOF and TOF analyses, the influence of the material budget on the matching of global tracks with hits in the TOF detector is computed by comparing the matching efficiency for tracks traversing a different amount of material, in particular sectors with and without transition radiation detector (TRD) modules installed. In the HMPID analysis, the $d_{\mathrm{MIP-trk}}$ cut selection is varied to check its systematic effect on the matching of global tracks with HMPID signals.

In the kink analysis, the total systematic uncertainty is calculated as the quadratic sum of the contributions listed in Table 2. The kaon misidentification correction (1 − purity) described in Sect. 2.3.5, which is on average 2.1 %, depends on the relative particle abundances in the Monte-Carlo and a p_{T}-dependent uncertainty of about 2 % on the purity is estimated. The kink identification uncertainty (3 %, almost flat in the considered p_{T} region) is also estimated with Monte-Carlo simulations by comparing the results by varying slightly some parameters of the analysis: the fiducial volume of the TPC is increased from the nominal $130 < R < 200$ to $20 < R < 210$ cm, the q_{T} threshold is reduced from the nominal 120 to 40 MeV/c, and the requirement on the number of TPC clusters of the mother track is increased from the nominal 20 to 50 clusters.

The systematic uncertainty on the efficiency for findable kink vertices was estimated to be 3 % independently of p_{T} by comparing, in real data and Monte Carlo simulations, the number of raw reconstructed kinks per kink radius unit in two different fiducial volumes inside the TPC, namely 130–200 and 140–190 cm.

Finally, a systematic uncertainty common to each analysis is related to the normalisation to inelastic collisions. The normalisation factor was evaluated in [36] and it is $0.852^{+0.062}_{-0.030}$.

All described uncertainties are strongly correlated among the p_{T} bins. Most of the uncertainties (e.g. tracking efficiency, ITS–TPC matching, TOF matching, material budget or PID) are also correlated between the different particle species.

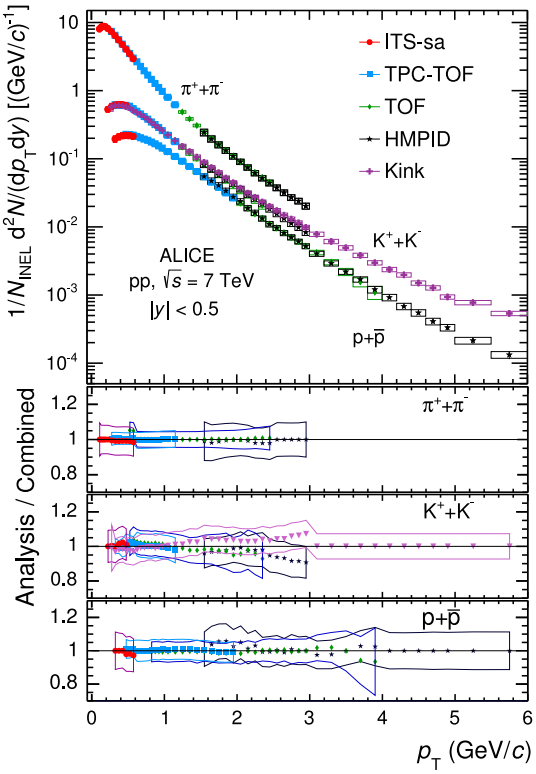

Fig. 12 *Top panel* p_{T} spectra of π, K and p, sum of particles and antiparticles, measured with ALICE at mid-rapidity ($|y| < 0.5$) in pp collisions at $\sqrt{s} = 7$ TeV by using different PID techniques. The spectra are normalised to the number of inelastic collisions. Statistical (*vertical error bars*) and systematic (*open boxes*) uncertainties are reported. The *horizontal width of the boxes* represents the p_{T}-bin width. The *markers* are placed at the bin *centre*. *Bottom panels* ratio between the spectra obtained from each analysis and the combined one. The *error bands* represent the total systematic uncertainties for each analysis. The uncertainty due to the normalisation to inelastic collisions ($^{+7}_{-4}$ %), common to the five PID analyses, is not included

3 Results

The mid-rapidity ($|y| < 0.5$) transverse momentum spectra of $\pi^+ + \pi^-$, $K^+ + K^-$ and $p + \overline{p}$ obtained with the five analysis techniques discussed in Sect. 2, normalised to the number of inelastic collisions N_{INEL}, are reported in the top panel of Fig. 12. For a given hadron species, the spectra of particles and antiparticles are found to be compatible within uncertainties. Therefore, all the spectra shown in this section are reported for summed charges. Since in their overlap p_{T} regions the spectra from the different PID techniques are consistent within uncertainties, they are averaged in a sequential procedure. The first step consists in averaging the two analyses whose results are the most closely correlated (namely TPC–TOF and TOF). Successively, the other analyses are added one-by-one to the running average according to their degree of correlation with the previous ones. At each step of this sequential procedure, a weighted average of two spectra is computed by using as weights the inverse of the squares of the uncorrelated systematic uncertainties. The uncorrelated and correlated uncertainties are propagated separately through the weighted average formula. In Fig. 13 the π, K and p spectra, resulting from the combination of the five analyses, are reported. The bottom panels of Fig. 12 show the ratios between the spectra from each analysis and the combined one: the former are considered with their total

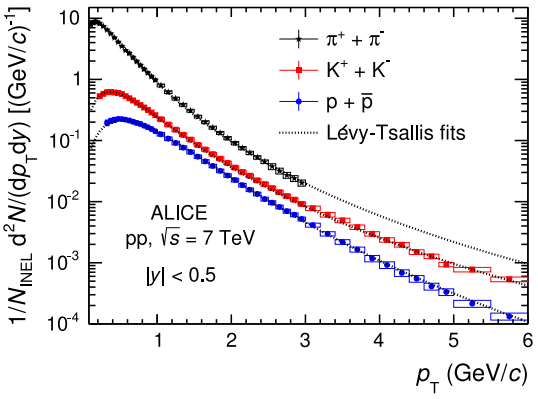

Fig. 13 Combined p_T spectra of π, K and p, sum of particles and antiparticles, measured with ALICE at mid-rapidity ($|y| < 0.5$) in pp collisions at $\sqrt{s} = 7$ TeV normalised to the number of inelastic collisions. Statistical (*vertical error bars*) and systematic (*open boxes*) uncertainties are reported. The uncertainty due to the normalisation to inelastic collisions ($^{+7}_{-4}$ %) is not shown. The spectra are fitted with Lévy–Tsallis functions

systematic uncertainties, the latter without uncertainty. The uncertainty due to the normalisation to inelastic collisions ($^{+7}_{-4}$ %), common to the five PID analyses, is not included. The agreement between each analysis and the combined one is satisfactory, being within the total systematic uncertainties.

To extrapolate to zero and infinite momentum, the combined spectra reported in Fig. 13 are fitted with the Lévy–Tsallis function [39,40]

$$\frac{\mathrm{d}^2N}{\mathrm{d}p_\mathrm{T}\mathrm{d}y} = p_\mathrm{T}\frac{\mathrm{d}N}{\mathrm{d}y}K\left(1+\frac{m_\mathrm{T}-m_0}{nC}\right)^{-n}, \tag{3}$$

where

$$K = \frac{(n-1)(n-2)}{nC(nC+m_0(n-2))}, \tag{4}$$

$m_\mathrm{T} = \sqrt{p_\mathrm{T}^2+m_0^2}$, m_0 is the particle rest mass and C, n and the yield $\mathrm{d}N/\mathrm{d}y$ are the free parameters. The Lévy–Tsallis function describes rather well the spectra. The χ^2 per number of degrees of freedom (ndf) of the fit are lower than unity (see Table 3) due to residual correlations in the point-to-point systematic uncertainties. In Table 3 the values of the p_T-integrated yield $\mathrm{d}N/\mathrm{d}y$ and of the mean transverse momentum $\langle p_\mathrm{T}\rangle$ are reported for each particle species. They are obtained using the measured data in the p_T range where they are available and the Lévy–Tsallis function fitted to the data elsewhere, to extrapolate to zero and infinite momentum. The lowest p_T experimentally accessible and the fraction of yield contained in the extrapolated region are also reported in the table. The extrapolation to infinite momentum gives a negligible contribution to the values of both $\mathrm{d}N/\mathrm{d}y$ and $\langle p_\mathrm{T}\rangle$. The $\mathrm{d}N/\mathrm{d}y$ and $\langle p_\mathrm{T}\rangle$ uncertainties reported in Table 3 are the combination of the statistical and the systematic ones. The statistical uncertainties are negligible, while the systematic uncertainties are the sum of two independent contributions. The first contribution is due to the systematic uncertainties on the measured p_T-differential yields and it was estimated by repeating the Lévy–Tsallis fits moving the measured points within their systematic uncertainties. The second contribution is due to the extrapolation to zero momentum and it is estimated using different fitting functions (namely modified Hagedorn [41] and UA1 parametrisation [42]). Results for positively and negatively charged particles, separately, are also reported. It should be noticed that the yields of particles and antiparticles are compatible within uncertainties.

In Fig. 14 the p_T spectra of identified charged hadrons, sum of particles and antiparticles, measured with ALICE at $\sqrt{s} = 7$ TeV are compared to the results obtained by the CMS Collaboration at the same centre-of-mass energy [17]. Even though the measurements are performed in different rapidity intervals ($|y| < 0.5$ for ALICE, $|y| < 1$ for CMS), they can be compared since the p_T spectra are essentially independent of rapidity for $|y| < 1$. A similar comparison at $\sqrt{s} = 0.9$ TeV is reported in [17]. At both energies, the ALICE spectra are normalised to the number of inelastic collisions, while the CMS results are normalised to the double-sided selection (at least one particle with $E > 3$ GeV in both $-5 < \eta < -3$ and $3 < \eta < 5$). An empirical scaling factor of 0.78, computed by the CMS Collaboration in [17] for the spectra measured in pp collisions at $\sqrt{s} = 0.9$ TeV, is therefore applied to the CMS data points at $\sqrt{s} = 7$ TeV, to take into account the different event selections (details are given in [17]). With this scaling, the pion and kaon spectra measured with ALICE and CMS are found to agree within uncertainties. The proton spectra have different slopes: for $p_\mathrm{T} < 1$ GeV/c the ALICE and CMS results agree within uncertainties, while at higher p_T a discrepancy of up to 20 % is observed.

In Fig. 15 the π, K and p integrated yields, $\mathrm{d}N/\mathrm{d}y$, are compared with similar measurements in the central rapidity region at various collision energies. In particular, results from ALICE at $\sqrt{s} = 900$ GeV [15] and $\sqrt{s} = 2.76$ TeV [16], PHENIX at $\sqrt{s} = 62.4$ GeV and $\sqrt{s} = 200$ GeV [18] and CMS, scaled by the empirical factor 0.78, at $\sqrt{s} = 900$ GeV, $\sqrt{s} = 2.76$ TeV and $\sqrt{s} = 7$ TeV [17] are shown. The $\mathrm{d}N/\mathrm{d}y$ values from PHENIX are reported for particles and antiparticles separately, while the results at large hadron collider (LHC) energies are the average between positively and negatively charged particles, since particle and antiparticle spectra are compatible at these energies. We notice that the CMS Collaboration does not include, in the systematic uncertainties associated to $\mathrm{d}N/\mathrm{d}y$ and $\langle p_\mathrm{T}\rangle$, the contribution due to the extrapolation to $p_\mathrm{T} = 0$. For this reason, in Figs. 16 and 17, the ALICE uncertainties are larger than the CMS

Table 3 dN/dy and $\langle p_{\mathrm{T}} \rangle$ extracted from Lévy–Tsallis fits to the measured π, K, p spectra in inelastic pp collisions at $\sqrt{s} = 7$ TeV for $|y| < 0.5$ with combined statistical and systematic uncertainties (statistical uncertainties are negligible) together with the p_{T} of the lowest experimentally accessible point (L. p_{T}) and the extrapolated fraction. The systematic uncertainty on dN/dy due to normalisation to inelastic collisions ($^{+7}_{-4}$ %) is not included

Particle	dN//dy	$\langle p_T \rangle$ (GeV/c)	χ^2/ndf	L. p_{T} (GeV/c)	Extr. (%)
$\pi^+ + \pi^-$	4.49 ± 0.20	0.466 ± 0.010	19.1/38	0.10	9
$K^+ + K^-$	0.572 ± 0.032	0.773 ± 0.016	5.0/45	0.20	10
$p + \overline{p}$	0.247 ± 0.018	0.900 ± 0.029	10.8/43	0.30	12
π^+	2.26 ± 0.10	0.464 ± 0.010	24.0/38	0.10	9
π^-	2.23 ± 0.10	0.469 ± 0.010	15.0/38	0.10	9
K^+	0.286 ± 0.016	0.777 ± 0.016	7.4/45	0.20	9
K^-	0.286 ± 0.016	0.770 ± 0.016	10.0/45	0.20	10
p	0.124 ± 0.009	0.900 ± 0.027	9.5/43	0.30	12
$\overline{p}$	0.123 ± 0.010	0.900 ± 0.032	12.3/43	0.30	12

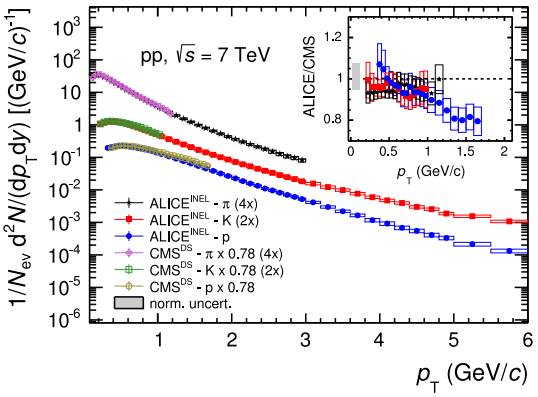

Fig. 14 Comparison of p_{T} spectra of π, K and p (sum of particles and antiparticles) measured by the ALICE ($|y| < 0.5$) and CMS Collaborations ($|y| < 1$) in pp collisions at $\sqrt{s} = 7$ TeV. The CMS data points are scaled by the empirical factor 0.78, as described in [17]. *Inset plot* ratios between ALICE and CMS data in the common p_{T} range. The combined ALICE and CMS statistical (*vertical error bars*) and systematic (*open boxes*) uncertainties are reported. The combined ALICE ($^{+7}_{-4}$ %) and CMS (±3 %) normalisation uncertainty is shown as a *grey box* around 1 and not included in the point-to-point uncertainties

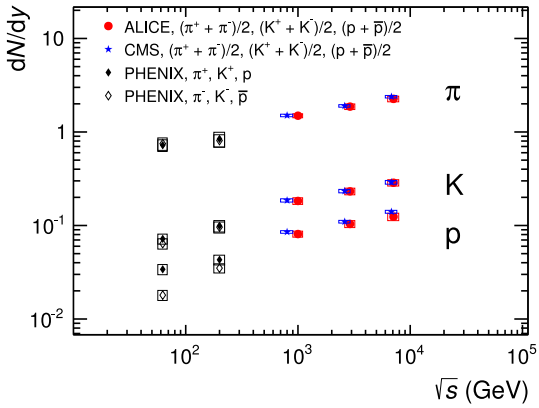

Fig. 15 p_{T}-integrated yields dN/dy of π, K and p as a function of the centre-of-mass energy in pp collisions. PHENIX results are for separate charges, while CMS and ALICE results are the average of the dN/dy of particles and antiparticles. ALICE and CMS points are slightly shifted along the x-axis for a better visualisation. *Errors* (*open boxes*) are the combination of statistical (negligible), systematic and normalisation uncertainties

ones. Similar results from the STAR Collaboration [43] are not included, here and in the following plots, since they are provided for non-single diffractive events and include contributions of feed-down from weak decays.

The $(K^+ + K^-)/(\pi^+ + \pi^-)$ and $(p + \overline{p})/(\pi^+ + \pi^-)$ ratios, as a function of the centre-of-mass energy, are shown in the top and bottom panels of Fig. 16, respectively. Results at mid-rapidity from ALICE at $\sqrt{s} = 0.9$, 2.76 [15,16] and 7 TeV, CMS at $\sqrt{s} = 0.9$, 2.76 and 7 TeV [17], PHENIX at $\sqrt{s} = 62.4$ and 200 GeV [18] and NA49 at $\sqrt{s} = 17.3$ GeV [19–21] are displayed. The ratio $(p + \overline{p})/(\pi^+ + \pi^-)$ from NA49, calculated from the measured particle yields, is not reported because the uncertainty cannot be computed from the results published in [19–21]. Results in proton–antiproton collisions from E735 at $\sqrt{s} = 0.3$, 0.54, 1 and 1.8 TeV [22,23] and UA5 at $\sqrt{s} = 0.2$, 0.546 and 0.9 TeV [24] are reported, but a direct comparison with them is not straightforward due to different baryon number in the initial state. The E735 Collaboration provides measurements only for $\overline{p}$ and not for p yields. Hence the proton-to-pion ratio is computed as $2\overline{p}/(\pi^+ + \pi^-)$. In addition, the E735 results for the proton-to-pion ratio are shown in Fig. 16 only for $\sqrt{s} = 1.8$ TeV because at the other energies the $\overline{p}$ spectra include contributions of feed-down from weak decays and are not directly comparable with the measurements provided by the other experiments. For $\sqrt{s} > 0.9$ TeV, no dependence on the centre-of-mass energy of the $(K^+ + K^-)/(\pi^+ + \pi^-)$ and $(p + \overline{p})/(\pi^+ + \pi^-)$ ratios is observed within uncertainties.

In Fig. 17 the average transverse momenta $\langle p_{\mathrm{T}} \rangle$ of pions, kaons and protons, extracted from the sum of particle and antiparticle spectra, as a function of the centre-of-mass

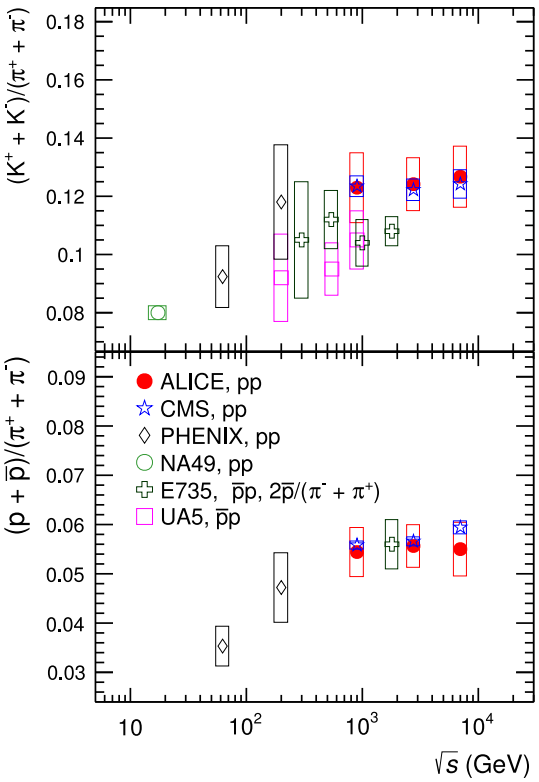

Fig. 16 $(K^+ + K^-)/(\pi^+ + \pi^-)$ (*top*) and $(p+\overline{p})/(\pi^+ + \pi^-)$ (*bottom*) ratios in pp and $p\overline{p}$ collisions as a function of the collision energy $\sqrt{s}$. *Errors* (*open boxes*) are the combination of statistical (negligible) and systematic uncertainties

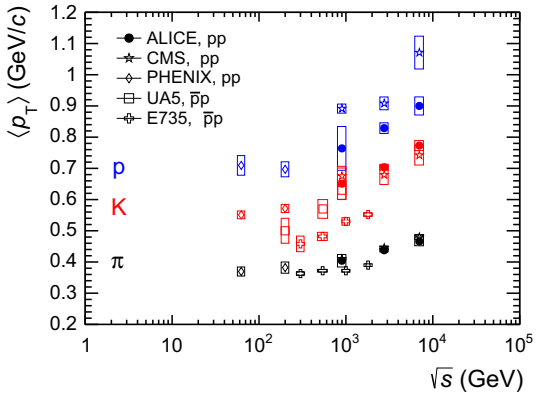

Fig. 17 $\langle p_T \rangle$ as a function of the centre-of-mass energy. *Errors* (*open boxes*) are the combination of statistical (negligible) and systematic uncertainties. Normalisation uncertainties are not included

energy are reported. Results at mid-rapidity in proton–proton collisions from ALICE at $\sqrt{s} = 0.9$, 2.76 [15,16] and 7 TeV, CMS at $\sqrt{s} = 0.9$, 2.76 and 7 TeV [17] and PHENIX at $\sqrt{s} =$ 62.4 and 200 GeV [18] are shown. In addition measurements obtained with E735 at $\sqrt{s} = 0.3$, 0.54, 1 and 1.8 TeV [22] and UA5 at $\sqrt{s} = 0.2$, 0.546, 0.9 TeV [24] in proton–antiproton collisions are also reported. The values of $\langle p_T \rangle$ of $\overline{p}$ from E735 are not shown since the spectra include contributions of feed-down from weak decays and hence are not directly comparable with the values provided by the other experiments. A slight increase of $\langle p_T \rangle$ with increasing centre-of-mass energy is observed. This rising trend is in particular apparent for $\sqrt{s} > 0.9$ TeV and it could be related to the increasing importance of hard processes at these energies. At $\sqrt{s} = 7$ TeV, the ALICE and CMS results are consistent within uncertainties except for the proton $\langle p_T \rangle$. This discrepancy is mostly due to the difference in the shape of the proton spectra seen in Fig. 14, rather than to the extrapolation to the unmeasured p_T range: a 13 % difference is observed on the $\langle p_T \rangle$ values calculated from the ALICE and CMS data points in the common p_T range.

4 Comparison to models

The comparison between the measured p_T spectra of π, K and p and the calculations of QCD-inspired Monte-Carlo event generators gives useful information on hadron production mechanisms. Figure 18 shows the comparison of the measured pion, kaon and proton p_T spectra, sum of particles and antiparticles, with two tunes of the PYTHIA6 generator (PYTHIA6-CentralPerugia2011 [26] and PYTHIA6-Z2 [27]),[1] PYTHIA8 tune 4Cx [2,3], EPOS LHC [4,5] and PHOJET [6].

These event generators are often used and tested to describe hadron collisions at high energies. PYTHIA is a general-purpose pQCD-based event generator, which uses a factorised perturbative expansion for the hardest parton–parton interaction, combined with parton showers and detailed models of hadronisation and multiparton interactions. All presented PYTHIA tunes use a colour reconnection mechanism [1] which can mimic effects similar to that induced by collective flow in Pb–Pb collisions [45]. In both PHOJET and EPOS, which are microscopic models that utilise the colour-exchange mechanism of string excitation, the hadronic interactions are treated in terms of Reggeon and Pomeron exchanges.

PYTHIA6-Z2 tune is based on the first measurement of multiplicity distributions in minimum-bias pp collisions at $\sqrt{s} = 900$ GeV at the LHC. In the CentralPerugia2011 tuning both LEP fragmentation functions and minimun-bias charged particle multiplicity and underlying event data from the LHC are used. Both PYTHIA8 and EPOS LHC are tuned to reproduce the existing data available from the LHC (e.g. multiplicity and, for EPOS, also identified hadron production up to 1

[1] The PYTHIA6 tunes are simulated using Rivet [44], a toolkit for validation of Monte-Carlo event generators.

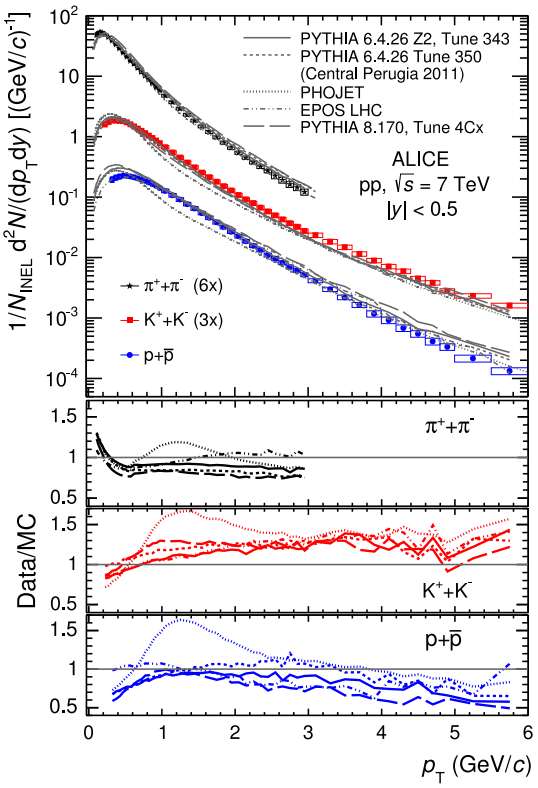

Fig. 18 *Top panel* measured p_T spectra of pions, kaons and protons, sum of particles and antiparticles, compared to PYTHIA6-Z2, PYTHIA6-CentralPerugia2011, PYTHIA8, EPOS LHC and PHOJET Monte-Carlo calculations. Statistical (*vertical error bars*) and systematic (*open boxes*) uncertainties are reported for the measured spectra. *Bottom panels* ratios between data and Monte-Carlo calculations

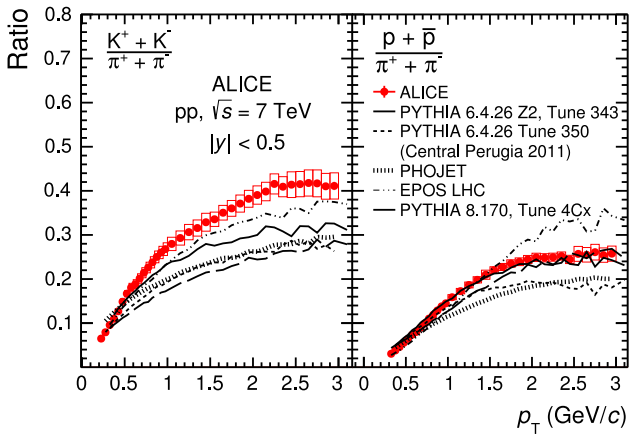

Fig. 19 Measured $(K^+ + K^-)/(\pi^+ + \pi^-)$ (*left*) and $(p + \overline{p})/(\pi^+ + \pi^-)$ (*right*) ratios as a function of p_T compared to PYTHIA6-Z2, PYTHIA6-CentralPerugia2011, PYTHIA8, EPOS LHC and PHOJET calculations. Statistical (*vertical error bars*) and systematic (*open boxes*) uncertainties are reported for the measured spectra

GeV/c for pions and kaons and up to 1.5 GeV/c for protons). The PHOJET parameters are not retuned using the LHC data.

The measured pion p_T spectrum is reproduced by EPOS within 15 % over the whole p_T range. PYTHIA6-Z2, PYTHIA6-CentralPerugia2011 and PYTHIA8 show similar trends. They correctly predict the shapes of the pion spectra for $p_T > 500$ MeV/c, overestimating the data by about 10, 20 and 25 %, respectively, while the shapes differ from data for $p_T < 200$ MeV/c (the ratios are not flat) and the yields are underestimated by up to 30 %. The PHOJET generator does not provide a satisfactory description of the measured spectrum shape for any of the particle species. The deviations from the data show a maximum for $p_T \sim 1.2$ GeV/c and are more pronounced for kaons and protons than for pions. All the tested Monte-Carlo generators underestimate the kaon yield by about 20–30 % for $p_T > 600$ MeV/c, while for $p_T < 400$ MeV/c they overestimate the data by up to 30 %. A similar deviation is observed by the ALICE Collaboration also for other strange particle species with a hierarchy depending on the strangeness content [46]. The proton yield is well described by EPOS only at low transverse momenta ($p_T < 1$ GeV/c), while the generator tends to overestimate the data by up to 30 % at higher p_T. None of the three PYTHIA tunes describes the shape of the proton spectrum in the full p_T range. All of them give a reasonable description of the yield in the range $1 < p_T < 2$ GeV/c, but they overestimate the data at lower and higher p_T by up to 40 %.

The comparison of the p_T-dependent particle ratios with models allows the hadronisation and soft parton interaction mechanisms implemented in the event generators to be tested. In the left and right panels of Fig. 19, the measured $(K^+ + K^-)/(\pi^+ + \pi^-)$ and $(p + \overline{p})/(\pi^+ + \pi^-)$ ratios as a function of p_T are compared with the same event generators shown in Fig. 18. The measured $(K^+ + K^-)/(\pi^+ + \pi^-)$ ratio increases from 0.05 at $p_T = 0.2$ GeV/c up to 0.45 at $p_T \sim 3$ GeV/c with a slope that decreases with increasing p_T. All the models underestimate the data at high momenta, with EPOS exhibiting the smallest deviation. The measured $(p + \overline{p})/(\pi^+ + \pi^-)$ shows an increase from 0.03 at $p_T = 0.3$ GeV/c up to 0.25 at $p_T \sim 1.5$ GeV/c, while above this p_T it tends to flatten. The data are well described by PYTHIA6-Z2, while PYTHIA6-CentralPerugia2011, PHOJET and EPOS show a large deviation at high momenta. PYTHIA8 shows a smaller deviation over the whole momentum range even if, as seen in Fig. 18, it overestimates both pion and proton spectra.

The comparison between data and Monte-Carlo calculations shows that the tunes of the generators based only on few global observables, such as the integrated charged hadron multiplicity, allow only for a partial description of the data. The high-precision measurements of the identified charged hadron p_T spectra reported here, which cover a wide momentum range in the central rapidity region, give useful information for a fine tuning of the Monte-Carlo generators and a better understanding of soft particle production mechanisms at LHC energies.

5 Summary

A detailed analysis of primary $\pi^{\pm}$, $K^{\pm}$, p and $\overline{p}$ production in proton–proton collisions at $\sqrt{s} = 7$ TeV with the ALICE detector has been performed. Particle identification is performed using several techniques namely the specific ionisation energy loss measured in the ITS and TPC, the time of flight measured with the TOF detector, the Cherenkov radiation measured in the HMPID and the kink-topology identification of the weak decays of charged kaons. The combination of these techniques allows for precision measurements of the p_{T} spectra over a wide momentum range: from 0.1 up to 3 GeV/c for pions, from 0.2 up to 6 GeV/c for kaons and from 0.3 up to 6 GeV/c for protons. A comparison of the ALICE results with similar measurements performed by the PHENIX Collaboration at RHIC shows that the p_{T}-integrated yields increase with collision energy for all the measured particle species. A slight increase of the $\langle p_{\mathrm{T}} \rangle$ with $\sqrt{s}$ is also observed. This rising trend that becomes apparent at $\sqrt{s} > 0.9$ TeV is established by the higher $\sqrt{s}$ LHC data. It could be related to the increasing importance of hard processes at these energies. The p_{T}-integrated K/π and p/π ratios extend the measurements available at lower collision energies from SPS, Sp$\overline{\mathrm{p}}$S and RHIC experiments showing a saturation above $\sqrt{s} = 0.9$ TeV. Finally, the p_{T} spectra and particle ratios have been compared with the calculations of QCD-inspired Monte-Carlo models namely PYTHIA6-Z2, PYTHIA6-CentralPerugia2011, PYTHIA8, EPOS LHC and PHOJET. Even though the shapes of the spectra are fairly well reproduced by all models (except PHOJET that fails to describe the spectrum shape of all the three hadron species), none of them can describe simultaneously the measured yields of pions, kaons and protons. These results can be used for a better understanding of the hadron production mechanisms in pp interactions at LHC energies and could further constrain the parameters of the models.

Acknowledgments The ALICE Collaboration would like to thank all its engineers and technicians for their invaluable contributions to the construction of the experiment and the CERN accelerator teams for the outstanding performance of the LHC complex. The ALICE Collaboration gratefully acknowledges the resources and support provided by all Grid centres and the Worldwide LHC Computing Grid (WLCG) Collaboration. The ALICE Collaboration acknowledges the following funding agencies for their support in building and running the ALICE detector: State Committee of Science, World Federation of Scientists (WFS) and Swiss Fonds Kidagan, Armenia, Conselho Nacional de Desenvolvimento Científico e Tecnológico (CNPq), Financiadora de Estudos e Projetos (FINEP), Fundação de Amparo à Pesquisa do Estado de São Paulo (FAPESP); National Natural Science Foundation of China (NSFC), the Chinese Ministry of Education (CMOE) and the Ministry of Science and Technology of China (MSTC); Ministry of Education and Youth of the Czech Republic; Danish Natural Science Research Council, the Carlsberg Foundation and the Danish National Research Foundation; The European Research Council under the European Community's Seventh Framework Programme; Helsinki Institute of Physics and the Academy of Finland; French CNRS-IN2P3, the 'Region Pays de Loire', 'Region Alsace', 'Region Auvergne' and CEA, France; German Bundesministerium fur Bildung, Wissenschaft, Forschung und Technologie (BMBF) and the Helmholtz Association; General Secretariat for Research and Technology, Ministry of Development, Greece; Hungarian Orszagos Tudomanyos Kutatasi Alappgrammok (OTKA) and National Office for Research and Technology (NKTH); Department of Atomic Energy and Department of Science and Technology of the Government of India; Istituto Nazionale di Fisica Nucleare (INFN) and Centro Fermi – Museo Storico della Fisica e Centro Studi e Ricerche "Enrico Fermi", Italy; MEXT Grant-in-Aid for Specially Promoted Research, Japan; Joint Institute for Nuclear Research, Dubna; National Research Foundation of Korea (NRF); Consejo Nacional de Cienca y Tecnologia (CONACYT), Direccion General de Asuntos del Personal Academico (DGAPA), México; Amerique Latine Formation academique European Commission (ALFA-EC) and the EPLANET Program (European Particle Physics Latin American Network) Stichting voor Fundamenteel Onderzoek der Materie (FOM) and the Nederlandse Organisatie voor Wetenschappelijk Onderzoek (NWO), Netherlands; Research Council of Norway (NFR); National Science Centre, Poland; Ministry of National Education/Institute for Atomic Physics and Consiliul National al Cercettrii tiinifice – Executive Agency for Higher Education Research Development and Innovation Funding (CNCS-UEFISCDI) – Romania; Ministry of Education and Science of Russian Federation, Russian Academy of Sciences, Russian Federal Agency of Atomic Energy, Russian Federal Agency for Science and Innovations and The Russian Foundation for Basic Research; Ministry of Education of Slovakia; Department of Science and Technology, South Africa; Centro de Investigaciones Energeticas, Medioambientales y Tecnologicas (CIEMAT), E-Infrastructure shared between Europe and Latin America (EELA), Ministerio de Economía y Competitividad (MINECO) of Spain, Xunta de Galicia (Consellería de Educación), Centro de Aplicaciones Tecnolgicas y Desarrollo Nuclear (CEADEN), Cubaenergía, Cuba, and IAEA (International Atomic Energy Agency); Swedish Research Council (VR) and Knut and Alice Wallenberg Foundation (KAW); Ukraine Ministry of Education and Science; United Kingdom Science and Technology Facilities Council (STFC); The United States Department of Energy, the United States National Science Foundation, the State of Texas, and the State of Ohio; Ministry of Science, Education and Sports of Croatia and Unity through Knowledge Fund, Croatia. Council of Scientific and Industrial Research (CSIR), New Delhi, India.

Funded by SCOAP[3].

References

1. T. Sjöstrand, S. Mrenna, P.Z. Skands, PYTHIA 6.4 physics and manual. JHEP **0605**, 026 (2006). arXiv:hep-ph/0603175
2. T. Sjöstrand, S. Mrenna, P.Z. Skands, A brief introduction to PYTHIA 8.1. Comput. Phys. Commun. **178**, 852–867 (2008). arXiv:0710.3820 [hep-ph]
3. R. Corke, T. Sjöstrand, Multiparton interactions with an x-dependent proton size. JHEP **1105**, 009 (2011). arXiv:1101.5953 [hep-ph]
4. T. Pierog, I. Karpenko, J. Katzy, E. Yatsenko, K. Werner, EPOS LHC : test of collective hadronization with LHC data. arXiv:1306.0121 [hep-ph]
5. K. Werner, I. Karpenko, T. Pierog, M. Bleicher, K. Mikhailov, Event-by-event simulation of the three-dimensional hydrodynamic

evolution from flux tube initial conditions in ultra relativistic heavy ion collisions. Phys. Rev. C **82**, 044904 (2010). arXiv:1004.0805 [nucl-th]
6. R. Engel, J. Ranft, S. Roesler, Hard diffraction in hadron–hadron interactions and in photoproduction. Phys. Rev. D **52**, 1459–1468 (1995). arXiv:hep-ph/9502319
7. ALICE Collaboration, F. Carminati et al., ALICE: physics performance report, volume I. J. Phys. G **30**, 1517–1763 (2004)
8. ALICE Collaboration, B. Alessandro et al., ALICE: physics performance report, volume II. J. Phys. G **32**, 1295–2040 (2006)
9. ALICE Collaboration, B.B. Abelev et al., Performance of the ALICE experiment at the CERN LHC. Int. J. Mod. Phys. A **29**, 1430044 (2014). arXiv:1402.4476 [nucl-ex]
10. ALICE Collaboration, K. Aamodt et al., The ALICE experiment at the CERN LHC. JINST **3**, S08002 (2008)
11. ALICE Collaboration, K. Aamodt et al., Alignment of the ALICE inner tracking system with cosmic-ray tracks. JINST **5**, P03003 (2010). arXiv:1001.0502 [physics.ins-det]
12. J. Alme, Y. Andres, H. Appelshauser, S. Bablok, N. Bialas et al., The ALICE TPC, a large 3-dimensional tracking device with fast readout for ultra-high multiplicity events. Nucl. Instrum. Methods A **622**, 316–367 (2010). arXiv:1001.1950 [physics.ins-det]
13. A. Akindinov, A. Alici, A. Agostinelli, P. Antonioli, S. Arcelli et al., Performance of the ALICE time-of-flight detector at the LHC. Eur. Phys. J. Plus **128**, 44 (2013)
14. ALICE Collaboration, P. Martinengo, The ALICE high momentum particle identification system: an overview after the first large hadron collider run. Nucl. Instrum. Methods A **639**, 7–10 (2011)
15. ALICE Collaboration, K. Aamodt et al., Production of pions, kaons and protons in pp collisions at $\sqrt{s} = 900$ GeV with ALICE at the LHC. Eur. Phys. J. C **71**, 1655 (2011). arXiv:1101.4110 [hep-ex]
16. ALICE Collaboration, B.B. Abelev et al., Production of charged pions, kaons and protons at large transverse momenta in pp and PbPb collisions at $\sqrt{s_{\rm NN}} = 2.76$ TeV. Phys. Lett. B **736**, 196–207 (2014). arXiv:1401.1250 [nucl-ex]
17. CMS Collaboration, S. Chatrchyan et al., Study of the inclusive production of charged pions, kaons, and protons in pp collisions at $\sqrt{s} = 0.9$, 2.76, and 7 TeV. Eur. Phys. J. **C72**, 2164 (2012). arXiv:1207.4724 [hep-ex]
18. PHENIX Collaboration, A. Adare et al., Identified charged hadron production in $p + p$ collisions at $\sqrt{s} = 200$ and 62.4 GeV. Phys. Rev. C **83**, 064903 (2011). arXiv:1102.0753 [nucl-ex]
19. NA49 Collaboration, C. Alt et al., Inclusive production of charged pions in $p + p$ collisions at 158-GeV/c beam momentum. Eur. Phys. J. C **45**, 343–381 (2006). arXiv:hep-ex/0510009
20. NA49 Collaboration, T. Anticic et al., Inclusive production of charged kaons in $p + p$ collisions at 158 GeV/c beam momentum and a new evaluation of the energy dependence of kaon production up to collider energies. Eur. Phys. J. C **68**, 1–73 (2010). arXiv:1004.1889 [hep-ex]
21. NA49 Collaboration, T. Anticic et al., Inclusive production of protons, anti-protons and neutrons in $p + p$ collisions at 158-GeV/c beam momentum. Eur. Phys. J. C **65**, 9–63 (2010). arXiv:0904.2708 [hep-ex]
22. E735 Collaboration, T. Alexopoulos et al., Mass identified particle production in $p\bar{p}$ collisions at $\sqrt{s} = 300$-GeV, 540-GeV, 1000-GeV, and 1800-GeV. Phys. Rev. D **48**, 984–997 (1993)
23. T. Alexopoulos, C. Allen, E. Anderson, V. Balamurali, S. Banerjee et al., Hyperon production from $p\bar{p}$ collisions at $\sqrt{s} = 1.8$-TeV. FNAL-735 experiment. Phys. Rev. D **46**, 2773–2786 (1992)
24. UA5 Collaboration, R. Ansorge et al., Kaon production at 200-GeV and 900-GeV center-of-mass energy. Phys. Lett. B **199**, 311–316 (1987)
25. R. Aaij et al., Measurement of prompt hadron production ratios in pp collisions at $\sqrt{s} = 0.9$ and 7 TeV. Eur. Phys. J. C **72**, 2168 (2012). doi:10.1140/epjc/s10052-012-2168-x
26. P.Z. Skands, Tuning Monte Carlo generators: the Perugia tunes. Phys. Rev. D **82**, 074018 (2010). arXiv:1005.3457 [hep-ph]
27. R. Field, Early LHC underlying event data – findings and surprises, arXiv:1010.3558 [hep-ph]
28. ALICE Collaboration, E. Abbas et al., Performance of the ALICE VZERO system. JINST **8**, P10016 (2013). arXiv:1306.3130 [nucl-ex]
29. ALICE Collaboration, B. Abelev et al., Measurement of charm production at central rapidity in proton–proton collisions at $\sqrt{s} = 7$ TeV. JHEP **1201**, 128 (2012). arXiv:1111.1553 [hep-ex]
30. ALICE Collaboration, B. Abelev et al., Centrality dependence of π, K, p production in Pb–Pb collisions at $\sqrt{s_{NN}} = 2.76$ TeV. Phys. Rev. C **88**(4), 044910 (2013). arXiv:1303.0737 [hep-ex]
31. PHOBOS Collaboration, B. Back et al., Identified hadron transverse momentum spectra in Au + Au collisions at $\sqrt{s_{NN}} = 62.4$-GeV. Phys. Rev. C **75**, 024910 (2007). arXiv:nucl-ex/0610001
32. L. Rolandi, W. Riegler, W. Blum, Particle Detection with Drift Chambers (Springer, Berlin, 2008). doi:10.1007/978-3-540-76684-1
33. ALICE Collaboration, D. Di Bari, The pattern recognition method for the CsI-RICH detector in ALICE. Nucl. Instrum. Methods A **502**, 300–304 (2003)
34. R. Brun, F. Carminati, S. Giani, GEANT detector description and simulation tool, CERN-W5013 (1994)
35. G. Battistoni, S. Muraro, P.R. Sala, F. Cerutti, A. Ferrari et al., The FLUKA code: description and benchmarking. AIP Conf. Proc. **896**, 31–49 (2007)
36. ALICE Collaboration, B. Abelev et al., Measurement of inelastic, single- and double-diffraction cross sections in proton–proton collisions at the LHC with ALICE. Eur. Phys. J. C **73**(6), 2456 (2013). arXiv:1208.4968 [hep-ex]
37. Particle Data Group Collaboration, J. Beringer et al., Review of particle physics (RPP). Phys. Rev. D **86**, 010001 (2012)
38. ALICE Collaboration, B. Abelev et al., Neutral pion and η meson production in proton–proton collisions at $\sqrt{s} = 0.9$ TeV and $\sqrt{s} = 7$ TeV. Phys. Lett. B **717**, 162–172 (2012). arXiv:1205.5724 [hep-ex]
39. C. Tsallis, Possible generalization of Boltzmann–Gibbs statistics. J. Stat. Phys. **52**, 479–487 (1988)
40. STAR Collaboration, B. Abelev et al., Strange particle production in p+p collisions at $\sqrt{s}$ = 200-GeV. Phys. Rev. C **75**, 064901 (2007). arXiv:nucl-ex/0607033
41. PHENIX Collaboration, A. Adare et al., Detailed measurement of the e^+e^- pair continuum in $p + p$ and Au + Au collisions at $\sqrt{s_{NN}} = 200$ GeV and implications for direct photon production. Phys. Rev. C **81**, 034911 (2010). arXiv:0912.0244 [nucl-ex]
42. UA1 Collaboration, C. Albajar et al., A study of the general characteristics of $p\bar{p}$ collisions at $\sqrt{s} = 0.2$-TeV to 0.9-TeV. Nucl. Phys. B **335**, 261 (1990)
43. STAR Collaboration, B. Abelev et al., Systematic measurements of identified particle spectra in pp, d^+ Au and Au + Au Collisions from STAR. Phys. Rev. C **79**, 034909 (2009). arXiv:0808.2041 [nucl-ex]
44. A. Buckley, J. Butterworth, L. Lonnblad, D. Grellscheid, H. Hoeth et al., Rivet user manual. Comput. Phys. Commun. **184**, 2803–2819 (2013). arXiv:1003.0694 [hep-ph]
45. A. Ortiz Velasquez, P. Christiansen, E. Cuautle Flores, I. Maldonado Cervantes, G. Pai, Color reconnection and flowlike patterns in pp Collisions. Phys. Rev. Lett. **111**(4), 042001 (2013). arXiv:1303.6326 [hep-ph]
46. ALICE Collaboration, B. Abelev et al., Multi-strange baryon production in pp collisions at $\sqrt{s} = 7$ TeV with ALICE. Phys. Lett. B **712**, 309–318 (2012). arXiv:1204.0282 [nucl-ex]

ALICE Collaboration

J. Adam[40], D. Adamová[83], M. M. Aggarwal[87], G. Aglieri Rinella[36], M. Agnello[111], N. Agrawal[48], Z. Ahammed[131], I. Ahmed[16], S. U. Ahn[68], I. Aimo[94,111], S. Aiola[136], M. Ajaz[16], A. Akindinov[58], S. N. Alam[131], D. Aleksandrov[100], B. Alessandro[111], D. Alexandre[102], R. Alfaro Molina[64], A. Alici[12,105], A. Alkin[3], J. Alme[38], T. Alt[43], S. Altinpinar[18], I. Altsybeev[130], C. Alves Garcia Prado[119], C. Andrei[78], A. Andronic[97], V. Anguelov[93], J. Anielski[54], T. Antičić[98], F. Antinori[108], P. Antonioli[105], L. Aphecetche[113], H. Appelshäuser[53], S. Arcelli[28], N. Armesto[17], R. Arnaldi[111], T. Aronsson[136], I. C. Arsene[22], M. Arslandok[53], A. Augustinus[36], R. Averbeck[97], M. D. Azmi[19], M. Bach[43], A. Badalà[107], Y. W. Baek[44], S. Bagnasco[111], R. Bailhache[53], R. Bala[90], A. Baldisseri[15], M. Ball[92], F. Baltasar Dos Santos Pedrosa[36], R. C. Baral[61], A. M. Barbano[111], R. Barbera[29], F. Barile[33], G. G. Barnaföldi[135], L. S. Barnby[102], V. Barret[70], P. Bartalini[7], J. Bartke[116], E. Bartsch[53], M. Basile[28], N. Bastid[70], S. Basu[131], B. Bathen[54], G. Batigne[113], A. Batista Camejo[70], B. Batyunya[66], P. C. Batzing[22], I. G. Bearden[80], H. Beck[53], C. Bedda[111], N. K. Behera[48,49], I. Belikov[55], F. Bellini[28], H. Bello Martinez[2], R. Bellwied[121], R. Belmont[134], E. Belmont-Moreno[64], V. Belyaev[76], G. Bencedi[135], S. Beole[27], I. Berceanu[78], A. Bercuci[78], Y. Berdnikov[85], D. Berenyi[135], R. A. Bertens[57], D. Berzano[27,36], L. Betev[36], A. Bhasin[90], I. R. Bhat[90], A. K. Bhati[87], B. Bhattacharjee[45], J. Bhom[127], L. Bianchi[27,121], N. Bianchi[72], C. Bianchin[57,134], J. Bielčík[40], J. Bielčíková[83], A. Bilandzic[80], S. Biswas[79], S. Bjelogrlic[57], F. Blanco[10], D. Blau[100], C. Blume[53], F. Bock[74,93], A. Bogdanov[76], H. Bøggild[80], L. Boldizsár[135], M. Bombara[41], J. Book[53], H. Borel[15], A. Borissov[96], M. Borri[82], F. Bossú[65], M. Botje[81], E. Botta[27], S. Böttger[52], P. Braun-Munzinger[97], M. Bregant[119], T. Breitner[52], T. A. Broker[53], T. A. Browning[95], M. Broz[40], E. J. Brucken[46], E. Bruna[111], G. E. Bruno[33], D. Budnikov[99], H. Buesching[53], S. Bufalino[36,111], P. Buncic[36], O. Busch[93], Z. Buthelezi[65], J. T. Buxton[20], D. Caffarri[30,36], X. Cai[7], H. Caines[136], L. Calero Diaz[72], A. Caliva[57], E. Calvo Villar[103], P. Camerini[26], F. Carena[36], W. Carena[36], J. Castillo Castellanos[15], A. J. Castro[124], E. A. R. Casula[25], C. Cavicchioli[36], C. Ceballos Sanchez[9], J. Cepila[40], P. Cerello[111], B. Chang[122], S. Chapeland[36], M. Chartier[123], J. L. Charvet[15], S. Chattopadhyay[131], S. Chattopadhyay[101], V. Chelnokov[3], M. Cherney[86], C. Cheshkov[129], B. Cheynis[129], V. Chibante Barroso[36], D. D. Chinellato[120], P. Chochula[36], K. Choi[96], M. Chojnacki[80], S. Choudhury[131], P. Christakoglou[81], C. H. Christensen[80], P. Christiansen[34], T. Chujo[127], S. U. Chung[96], C. Cicalo[106], L. Cifarelli[12,28], F. Cindolo[105], J. Cleymans[89], F. Colamaria[33], D. Colella[33], A. Collu[25], M. Colocci[28], G. Conesa Balbastre[71], Z. Conesa del Valle[51], M. E. Connors[136], J. G. Contreras[11,40], T. M. Cormier[84], Y. Corrales Morales[27], I. Cortés Maldonado[2], P. Cortese[32], M. R. Cosentino[119], F. Costa[36], P. Crochet[70], R. Cruz Albino[11], E. Cuautle[63], L. Cunqueiro[36], T. Dahms[37,92], A. Dainese[108], A. Danu[62], D. Das[101], I. Das[51,101], S. Das[4], A. Dash[120], S. Dash[48], S. De[119], A. De Caro[12,31], G. de Cataldo[104], J. de Cuveland[43], A. De Falco[25], D. De Gruttola[12,31], N. De Marco[111], S. De Pasquale[31], A. Deisting[93,97], A. Deloff[77], E. Dénes[135], G. D'Erasmo[33], D. Di Bari[33], A. Di Mauro[36], P. Di Nezza[72], M. A. Diaz Corchero[10], T. Dietel[89], P. Dillenseger[53], R. Divià[36], Ø. Djuvsland[18], A. Dobrin[57,81], T. Dobrowolski[77,a], D. Domenicis Gimenez[119], B. Dönigus[53], O. Dordic[22], A. K. Dubey[131], A. Dubla[57], L. Ducroux[129], P. Dupieux[70], R. J. Ehlers[136], D. Elia[104], H. Engel[52], B. Erazmus[36,113], F. Erhardt[128], D. Eschweiler[43], B. Espagnon[51], M. Estienne[113], S. Esumi[127], J. Eum[96], D. Evans[102], S. Evdokimov[112], G. Eyyubova[40], L. Fabbietti[37,92], D. Fabris[108], J. Faivre[71], A. Fantoni[72], M. Fasel[74], L. Feldkamp[54], D. Felea[62], A. Feliciello[111], G. Feofilov[130], J. Ferencei[83], A. Fernández Téllez[2], E. G. Ferreiro[17], A. Ferretti[27], A. Festanti[30], J. Figiel[116], M. A. S. Figueredo[123], S. Filchagin[99], D. Finogeev[56], F. M. Fionda[104], E. M. Fiore[33], M. G. Fleck[93], M. Floris[36], S. Foertsch[65], P. Foka[97], S. Fokin[100], E. Fragiacomo[110], A. Francescon[30,36], U. Frankenfeld[97], U. Fuchs[36], C. Furget[71], A. Furs[56], M. Fusco Girard[31], J. J. Gaardhøje[80], M. Gagliardi[27], A. M. Gago[103], M. Gallio[27], D. R. Gangadharan[74], P. Ganoti[88], C. Gao[7], C. Garabatos[97], E. Garcia-Solis[13], C. Gargiulo[36], P. Gasik[37,92], M. Germain[113], A. Gheata[36], M. Gheata[36,62], P. Ghosh[131], S. K. Ghosh[4], P. Gianotti[72], P. Giubellino[36], P. Giubilato[30], E. Gladysz Dziadus[116], P. Glässel[93], A. Gomez Ramirez[52], P. González Zamora[10], S. Gorbunov[43], L. Görlich[116], S. Gotovac[115], V. Grabski[64], L. K. Graczykowski[133], A. Grelli[57], A. Grigoras[36], C. Grigoras[36], V. Grigoriev[76], A. Grigoryan[1], S. Grigoryan[66], B. Grinyov[3], N. Grion[110], J. F. Grosse-Oetringhaus[36], J.-Y. Grossiord[129], R. Grosso[36], F. Guber[56], R. Guernane[71], B. Guerzoni[28], K. Gulbrandsen[80], H. Gulkanyan[1], T. Gunji[126], A. Gupta[90], R. Gupta[90], R. Haake[54], Ø. Haaland[18], C. Hadjidakis[51], M. Haiduc[62], H. Hamagaki[126], G. Hamar[135], L. D. Hanratty[102], A. Hansen[80], J. W. Harris[136], H. Hartmann[43], A. Harton[13], D. Hatzifotiadou[105], S. Hayashi[126], S. T. Heckel[53], M. Heide[54], H. Helstrup[38], A. Herghelegiu[78], G. Herrera Corral[11], B. A. Hess[35], K. F. Hetland[38], T. E. Hilden[46], H. Hillemanns[36], B. Hippolyte[55], P. Hristov[36], M. Huang[18], T. J. Humanic[20], N. Hussain[45], T. Hussain[19], D. Hutter[43], D. S. Hwang[21], R. Ilkaev[99], I. Ilkiv[77], M. Inaba[127], C. Ionita[36], M. Ippolitov[76,100], M. Irfan[19], M. Ivanov[97], V. Ivanov[85], V. Izucheev[112], P. M. Jacobs[74], C. Jahnke[119], H. J. Jang[68], M. A. Janik[133], P. H. S. Y. Jayarathna[121], C. Jena[30], S. Jena[121], R. T. Jimenez Bustamante[63], P. G. Jones[102], H. Jung[44], A. Jusko[102], P. Kalinak[59], A. Kalweit[36], J. Kamin[53], J. H. Kang[137], V. Kaplin[76], S. Kar[131], A. Karasu Uysal[69], O. Karavichev[56], T. Karavicheva[56], E. Karpechev[56], U. Kebschull[52], R. Keidel[138], D. L. D. Keijdener[57],

M. Keil[36], K. H. Khan[16], M. M. Khan[19], P. Khan[101], S. A. Khan[131], A. Khanzadeev[85], Y. Kharlov[112], B. Kileng[38], B. Kim[137], D. W. Kim[44,68], D. J. Kim[122], H. Kim[137], J. S. Kim[44], M. Kim[44], M. Kim[137], S. Kim[21], T. Kim[137], S. Kirsch[43], I. Kisel[43], S. Kiselev[58], A. Kisiel[133], G. Kiss[135], J. L. Klay[6], C. Klein[53], J. Klein[93], C. Klein-Bösing[54], A. Kluge[36], M. L. Knichel[93], A. G. Knospe[117], T. Kobayashi[127], C. Kobdaj[114], M. Kofarago[36], M. K. Köhler[97], T. Kollegger[43,97], A. Kolojvari[130], V. Kondratiev[130], N. Kondratyeva[76], E. Kondratyuk[112], A. Konevskikh[56], C. Kouzinopoulos[36], O. Kovalenko[77], V. Kovalenko[130], M. Kowalski[36,116], S. Kox[71], G. Koyithatta Meethaleveedu[48], J. Kral[122], I. Králik[59], A. Kravčáková[41], M. Krelina[40], M. Kretz[43], M. Krivda[59,102], F. Krizek[83], E. Kryshen[36], M. Krzewicki[43,97], A. M. Kubera[20], V. Kučera[83], Y. Kucheriaev[100,a], T. Kugathasan[36], C. Kuhn[55], P. G. Kuijer[81], I. Kulakov[43], J. Kumar[48], L. Kumar[79,87], P. Kurashvili[77], A. Kurepin[56], A. B. Kurepin[56], A. Kuryakin[99], S. Kushpil[83], M. J. Kweon[50], Y. Kwon[137], S. L. La Pointe[111], P. La Rocca[29], C. Lagana Fernandes[119], I. Lakomov[36,51], R. Langoy[42], C. Lara[52], A. Lardeux[15], A. Lattuca[27], E. Laudi[36], R. Lea[26], L. Leardini[93], G. R. Lee[102], S. Lee[137], I. Legrand[36], J. Lehnert[53], R. C. Lemmon[82], V. Lenti[104], E. Leogrande[57], I. León Monzón[118], M. Leoncino[27], P. Lévai[135], S. Li[7,70], X. Li[14], J. Lien[42], R. Lietava[102], S. Lindal[22], V. Lindenstruth[43], C. Lippmann[97], M. A. Lisa[20], H. M. Ljunggren[34], D. F. Lodato[57], P. I. Loenne[18], V. R. Loggins[134], V. Loginov[76], C. Loizides[74], X. Lopez[70], E. López Torres[9], A. Lowe[135], X.-G. Lu[93], P. Luettig[53], M. Lunardon[30], G. Luparello[26,57], A. Maevskaya[56], M. Mager[36], S. Mahajan[90], S. M. Mahmood[22], A. Maire[55], R. D. Majka[136], M. Malaev[85], I. Maldonado Cervantes[63], L. Malinina[66], D. Mal'Kevich[58], P. Malzacher[97], A. Mamonov[99], L. Manceau[111], V. Manko[100], F. Manso[70], V. Manzari[36,104], M. Marchisone[27], J. Mareš[60], G. V. Margagliotti[26], A. Margotti[105], J. Margutti[57], A. Marín[97], C. Markert[117], M. Marquard[53], N. A. Martin[97], J. Martin Blanco[113], P. Martinengo[36], M. I. Martínez[2], G. Martínez García[113], M. Martinez Pedreira[36], Y. Martynov[3], A. Mas[119], S. Masciocchi[97], M. Masera[27], A. Masoni[106], L. Massacrier[113], A. Mastroserio[33], H. Masui[127], A. Matyja[116], C. Mayer[116], J. Mazer[124], M. A. Mazzoni[109], D. Mcdonald[121], F. Meddi[24], A. Menchaca-Rocha[64], E. Meninno[31], J. Mercado Pérez[93], M. Meres[39], Y. Miake[127], M. M. Mieskolainen[46], K. Mikhaylov[58,66], L. Milano[36], J. Milosevic[22,132], L. M. Minervini[23,104], A. Mischke[57], A. N. Mishra[49], D. Miśkowiec[97], J. Mitra[131], C. M. Mitu[62], N. Mohammadi[57], B. Mohanty[79,131], L. Molnar[55], L. Montaño Zetina[11], E. Montes[10], M. Morando[30], D. A. Moreira De Godoy[113], S. Moretto[30], A. Morreale[113], A. Morsch[36], V. Muccifora[72], E. Mudnic[115], D. Mühlheim[54], S. Muhuri[131], M. Mukherjee[131], H. Müller[36], J. D. Mulligan[136], M. G. Munhoz[119], S. Murray[65], L. Musa[36], J. Musinsky[59], B. K. Nandi[48], R. Nania[105], E. Nappi[104], M. U. Naru[16], C. Nattrass[124], K. Nayak[79], T. K. Nayak[131], S. Nazarenko[99], A. Nedosekin[58], L. Nellen[63], F. Ng[121], M. Nicassio[97], M. Niculescu[36,62], J. Niedziela[36], B. S. Nielsen[80], S. Nikolaev[100], S. Nikulin[100], V. Nikulin[85], F. Noferini[12,105], P. Nomokonov[66], G. Nooren[57], J. Norman[123], A. Nyanin[100], J. Nystrand[18], H. Oeschler[93], S. Oh[136], S. K. Oh[67], A. Ohlson[36], A. Okatan[69], T. Okubo[47], L. Olah[135], J. Oleniacz[133], A. C. Oliveira Da Silva[119], M. H. Oliver[136], J. Onderwaater[97], C. Oppedisano[111], A. Ortiz Velasquez[63], A. Oskarsson[34], J. Otwinowski[97,116], K. Oyama[93], M. Ozdemir[53], Y. Pachmayer[93], P. Pagano[31], G. Paić[63], C. Pajares[17], S. K. Pal[131], J. Pan[134], A. K. Pandey[48], D. Pant[48], V. Papikyan[1], G. S. Pappalardo[107], P. Pareek[49], W. J. Park[97], S. Parmar[87], A. Passfeld[54], V. Paticchio[104], B. Paul[101], T. Pawlak[133], T. Peitzmann[57], H. Pereira Da Costa[15], E. Pereira De Oliveira Filho[119], D. Peresunko[76,100], C. E. Pérez Lara[81], V. Peskov[53], Y. Pestov[5], V. Petráček[40], V. Petrov[112], M. Petrovici[78], C. Petta[29], S. Piano[110], M. Pikna[39], P. Pillot[113], O. Pinazza[36,105], L. Pinsky[121], D. B. Piyarathna[121], M. Płoskoń[74], M. Planinic[128], J. Pluta[133], S. Pochybova[135], P. L. M. Podesta-Lerma[118], M. G. Poghosyan[86], B. Polichtchouk[112], N. Poljak[128], W. Poonsawat[114], A. Pop[78], S. Porteboeuf-Houssais[70], J. Porter[74], J. Pospisil[83], S. K. Prasad[4], R. Preghenella[36,105], F. Prino[111], C. A. Pruneau[134], I. Pshenichnov[56], M. Puccio[111], G. Puddu[25], P. Pujahari[134], V. Punin[99], J. Putschke[134], H. Qvigstad[22], A. Rachevski[110], S. Raha[4], S. Rajput[90], J. Rak[122], A. Rakotozafindrabe[15], L. Ramello[32], R. Raniwala[91], S. Raniwala[91], S. S. Räsänen[46], B. T. Rascanu[53], D. Rathee[87], V. Razazi[25], K. F. Read[124], J. S. Real[71], K. Redlich[77], R. J. Reed[134], A. Rehman[18], P. Reichelt[53], M. Reicher[57], F. Reidt[36,93], X. Ren[7], R. Renfordt[53], A. R. Reolon[72], A. Reshetin[56], F. Rettig[43], J.-P. Revol[12], K. Reygers[93], V. Riabov[85], R. A. Ricci[73], T. Richert[34], M. Richter[22], P. Riedler[36], W. Riegler[36], F. Riggi[29], C. Ristea[62], A. Rivetti[111], E. Rocco[57], M. Rodríguez Cahuantzi[2,11], A. Rodriguez Manso[81], K. Røed[22], E. Rogochaya[66], D. Rohr[43], D. Röhrich[18], R. Romita[123], F. Ronchetti[72], L. Ronflette[113], P. Rosnet[70], A. Rossi[36], F. Roukoutakis[88], A. Roy[49], C. Roy[55], P. Roy[101], A. J. Rubio Montero[10], R. Rui[26], R. Russo[27], E. Ryabinkin[100], Y. Ryabov[85], A. Rybicki[116], S. Sadovsky[112], K. Šafařík[36], B. Sahlmuller[53], P. Sahoo[49], R. Sahoo[49], S. Sahoo[61], P. K. Sahu[61], J. Saini[131], S. Sakai[72], M. A. Saleh[134], C. A. Salgado[17], J. Salzwedel[20], S. Sambyal[90], V. Samsonov[85], X. Sanchez Castro[55], L. Šándor[59], A. Sandoval[64], M. Sano[127], G. Santagati[29], D. Sarkar[131], E. Scapparone[105], F. Scarlassara[30], R. P. Scharenberg[95], C. Schiaua[78], R. Schicker[93], C. Schmidt[97], H. R. Schmidt[35], S. Schuchmann[53], J. Schukraft[36], M. Schulc[40], T. Schuster[136], Y. Schutz[36,113], K. Schwarz[97], K. Schweda[97], G. Scioli[28], E. Scomparin[111], R. Scott[124], K. S. Seeder[119], J. E. Seger[86], Y. Sekiguchi[126], I. Selyuzhenkov[97], K. Senosi[65], J. Seo[67,96], E. Serradilla[10,64], A. Sevcenco[62], A. Shabanov[56], A. Shabetai[113], O. Shadura[3], R. Shahoyan[36], A. Shangaraev[112], A. Sharma[90], N. Sharma[61,124], K. Shigaki[47], K. Shtejer[9,27],

Y. Sibiriak[100], S. Siddhanta[106], K. M. Sielewicz[36], T. Siemiarczuk[77], D. Silvermyr[34,84], C. Silvestre[71], G. Simatovic[128], G. Simonetti[36], R. Singaraju[131], R. Singh[79], S. Singha[79,131], V. Singhal[131], B. C. Sinha[131], T. Sinha[101], B. Sitar[39], M. Sitta[32], T. B. Skaali[22], M. Slupecki[122], N. Smirnov[136], R. J. M. Snellings[57], T. W. Snellman[122], C. Søgaard[34], R. Soltz[75], J. Song[96], M. Song[137], Z. Song[7], F. Soramel[30], S. Sorensen[124], M. Spacek[40], E. Spiriti[72], I. Sputowska[116], M. Spyropoulou Stassinaki[88], B. K. Srivastava[95], J. Stachel[93], I. Stan[62], G. Stefanek[77], M. Steinpreis[20], E. Stenlund[34], G. Steyn[65], J. H. Stiller[93], D. Stocco[113], P. Strmen[39], A. A. P. Suaide[119], T. Sugitate[47], C. Suire[51], M. Suleymanov[16], R. Sultanov[58], M. Šumbera[83], T. J. M. Symons[74], A. Szabo[39], A. Szanto de Toledo[119,a], I. Szarka[39], A. Szczepankiewicz[36], M. Szymanski[133], J. Takahashi[120], N. Tanaka[127], M. A. Tangaro[33], J. D. Tapia Takaki[51,b], A. Tarantola Peloni[53], M. Tariq[19], M. G. Tarzila[78], A. Tauro[36], G. Tejeda Muñoz[2], A. Telesca[36], K. Terasaki[126], C. Terrevoli[25,30], B. Teyssier[129], J. Thäder[74,97], D. Thomas[117], R. Tieulent[129], A. R. Timmins[121], A. Toia[53], S. Trogolo[111], V. Trubnikov[3], W. H. Trzaska[122], T. Tsuji[126], A. Tumkin[99], R. Turrisi[108], T. S. Tveter[22], K. Ullaland[18], A. Uras[129], G. L. Usai[25], A. Utrobicic[128], M. Vajzer[83], M. Vala[59], L. Valencia Palomo[70], S. Vallero[27], J. Van Der Maarel[57], J. W. Van Hoorne[36], M. van Leeuwen[57], T. Vanat[83], P. Vande Vyvre[36], D. Varga[135], A. Vargas[2], M. Vargyas[122], R. Varma[48], M. Vasileiou[88], A. Vasiliev[100], A. Vauthier[71], V. Vechernin[130], A. M. Veen[57], M. Veldhoen[57], A. Velure[18], M. Venaruzzo[73], E. Vercellin[27], S. Vergara Limón[2], R. Vernet[8], M. Verweij[134], L. Vickovic[115], G. Viesti[30,a], J. Viinikainen[122], Z. Vilakazi[125], O. Villalobos Baillie[102], A. Vinogradov[100], L. Vinogradov[130], Y. Vinogradov[99], T. Virgili[31], V. Vislavicius[34], Y. P. Viyogi[131], A. Vodopyanov[66], M. A. Völkl[93], K. Voloshin[58], S. A. Voloshin[134], G. Volpe[36,135], B. von Haller[36], I. Vorobyev[37,92], D. Vranic[36,97], J. Vrláková[41], B. Vulpescu[70], A. Vyushin[99], B. Wagner[18], J. Wagner[97], H. Wang[57], M. Wang[7,113], Y. Wang[93], D. Watanabe[127], M. Weber[36,121], S. G. Weber[97], J. P. Wessels[54], U. Westerhoff[54], J. Wiechula[35], J. Wikne[22], M. Wilde[54], G. Wilk[77], J. Wilkinson[93], M. C. S. Williams[105], B. Windelband[93], M. Winn[93], C. G. Yaldo[134], Y. Yamaguchi[126], H. Yang[57], P. Yang[7], S. Yano[47], S. Yasnopolskiy[100], Z. Yin[7], H. Yokoyama[127], I.-K. Yoo[96], V. Yurchenko[3], I. Yushmanov[100], A. Zaborowska[133], V. Zaccolo[80], A. Zaman[16], C. Zampolli[105], H. J. C. Zanoli[119], S. Zaporozhets[66], A. Zarochentsev[130], P. Závada[60], N. Zaviyalov[99], H. Zbroszczyk[133], I. S. Zgura[62], M. Zhalov[85], H. Zhang[7,18], X. Zhang[74], Y. Zhang[7], C. Zhao[22], N. Zhigareva[58], D. Zhou[7], Y. Zhou[57,80], Z. Zhou[18], H. Zhu[7,18], J. Zhu[7,113], X. Zhu[7], A. Zichichi[12,28], A. Zimmermann[93], M. B. Zimmermann[36,54], G. Zinovjev[3], M. Zyzak[43]

[1] A.I. Alikhanyan National Science Laboratory (Yerevan Physics Institute) Foundation, Yerevan, Armenia
[2] Benemérita Universidad Autónoma de Puebla, Puebla, Mexico
[3] Bogolyubov Institute for Theoretical Physics, Kiev, Ukraine
[4] Department of Physics and Centre for Astroparticle Physics and Space Science (CAPSS), Bose Institute, Kolkata, India
[5] Budker Institute for Nuclear Physics, Novosibirsk, Russia
[6] California Polytechnic State University, San Luis Obispo, California, USA
[7] Central China Normal University, Wuhan, China
[8] Centre de Calcul de l'IN2P3, Villeurbanne, France
[9] Centro de Aplicaciones Tecnológicas y Desarrollo Nuclear (CEADEN), Havana, Cuba
[10] Centro de Investigaciones Energéticas Medioambientales y Tecnológicas (CIEMAT), Madrid, Spain
[11] Centro de Investigación y de Estudios Avanzados (CINVESTAV), Mexico City and Mérida, Mexico
[12] Centro Fermi-Museo Storico della Fisica e Centro Studi e Ricerche "Enrico Fermi", Rome, Italy
[13] Chicago State University, Chicago, IL, USA
[14] China Institute of Atomic Energy, Beijing, China
[15] Commissariat à l'Energie Atomique, IRFU, Saclay, France
[16] COMSATS Institute of Information Technology (CIIT), Islamabad, Pakistan
[17] Departamento de Física de Partículas and IGFAE, Universidad de Santiago de Compostela, Santiago de Compostela, Spain
[18] Department of Physics and Technology, University of Bergen, Mons, Norway
[19] Department of Physics, Aligarh Muslim University, Aligarh, India
[20] Department of Physics, Ohio State University, Columbus, OH, USA
[21] Department of Physics, Sejong University, Seoul, South Korea
[22] Department of Physics, University of Oslo, Oslo, Norway
[23] Dipartimento di Elettrotecnica ed Elettronica del Politecnico, Bari, Italy
[24] Dipartimento di Fisica dell'Università 'La Sapienza' and Sezione INFN, Rome, Italy
[25] Dipartimento di Fisica dell'Università and Sezione INFN, Cagliari, Italy
[26] Dipartimento di Fisica dell'Università and Sezione INFN, Trieste, Italy

[27] Dipartimento di Fisica dell'Università and Sezione INFN, Turin, Italy
[28] Dipartimento di Fisica e Astronomia dell'Università and Sezione INFN, Bologna, Italy
[29] Dipartimento di Fisica e Astronomia dell'Università and Sezione INFN, Catania, Italy
[30] Dipartimento di Fisica e Astronomia dell'Università and Sezione INFN, Padua, Italy
[31] Dipartimento di Fisica 'E.R. Caianiello' dell'Università and Gruppo Collegato INFN, Salerno, Italy
[32] Dipartimento di Scienze e Innovazione Tecnologica dell'Università del Piemonte Orientale and Gruppo Collegato INFN, Alessandria, Italy
[33] Dipartimento Interateneo di Fisica 'M. Merlin' and Sezione INFN, Bari, Italy
[34] Division of Experimental High Energy Physics, University of Lund, Lund, Sweden
[35] Eberhard Karls Universität Tübingen, Tübingen, Germany
[36] European Organization for Nuclear Research (CERN), Geneva, Switzerland
[37] Excellence Cluster Universe, Technische Universität München, Munich, Germany
[38] Faculty of Engineering, Bergen University College, Mons, Norway
[39] Faculty of Mathematics, Physics and Informatics, Comenius University, Bratislava, Slovakia
[40] Faculty of Nuclear Sciences and Physical Engineering, Czech Technical University in Prague, Prague, Czech Republic
[41] Faculty of Science, P.J. Šafárik University, Kosice, Slovakia
[42] Faculty of Technology, Buskerud and Vestfold University College, Vestfold, Norway
[43] Frankfurt Institute for Advanced Studies, Johann Wolfgang Goethe-Universität Frankfurt, Frankfurt, Germany
[44] Gangneung-Wonju National University, Gangneung, South Korea
[45] Department of Physics, Gauhati University, Guwahati, India
[46] Helsinki Institute of Physics (HIP), Helsinki, Finland
[47] Hiroshima University, Hiroshima, Japan
[48] Indian Institute of Technology Bombay (IIT), Mumbai, India
[49] Indian Institute of Technology Indore (IITI), Indore, India
[50] Inha University, Incheon, South Korea
[51] Institut de Physique Nucléaire d'Orsay (IPNO), Université Paris-Sud, CNRS-IN2P3, Orsay, France
[52] Institut für Informatik, Johann Wolfgang Goethe-Universität Frankfurt, Frankfurt, Germany
[53] Institut für Kernphysik, Johann Wolfgang Goethe-Universität Frankfurt, Frankfurt, Germany
[54] Institut für Kernphysik, Westfälische Wilhelms-Universität Münster, Münster, Germany
[55] Institut Pluridisciplinaire Hubert Curien (IPHC), Université de Strasbourg, CNRS-IN2P3, Strasbourg, France
[56] Institute for Nuclear Research, Academy of Sciences, Moscow, Russia
[57] Institute for Subatomic Physics of Utrecht University, Utrecht, The Netherlands
[58] Institute for Theoretical and Experimental Physics, Moscow, Russia
[59] Institute of Experimental Physics, Slovak Academy of Sciences, Kosice, Slovakia
[60] Institute of Physics, Academy of Sciences of the Czech Republic, Prague, Czech Republic
[61] Institute of Physics, Bhubaneswar, India
[62] Institute of Space Science (ISS), Bucharest, Romania
[63] Instituto de Ciencias Nucleares, Universidad Nacional Autónoma de México, Mexico City, Mexico
[64] Instituto de Física, Universidad Nacional Autónoma de México, Mexico City, Mexico
[65] iThemba LABS, National Research Foundation, Somerset West, South Africa
[66] Joint Institute for Nuclear Research (JINR), Dubna, Russia
[67] Konkuk University, Seoul, South Korea
[68] Korea Institute of Science and Technology Information, Daejeon, South Korea
[69] KTO Karatay University, Konya, Turkey
[70] Laboratoire de Physique Corpusculaire (LPC), Clermont Université, Université Blaise Pascal, CNRS-IN2P3, Clermont-Ferrand, France
[71] Laboratoire de Physique Subatomique et de Cosmologie, Université Grenoble-Alpes, CNRS-IN2P3, Grenoble, France
[72] Laboratori Nazionali di Frascati, INFN, Frascati, Italy
[73] Laboratori Nazionali di Legnaro, INFN, Legnaro, Italy
[74] Lawrence Berkeley National Laboratory, Berkeley, California, USA
[75] Lawrence Livermore National Laboratory, Livermore, CA, USA
[76] Moscow Engineering Physics Institute, Moscow, Russia
[77] National Centre for Nuclear Studies, Warsaw, Poland

[78] National Institute for Physics and Nuclear Engineering, Bucharest, Romania
[79] National Institute of Science Education and Research, Bhubaneswar, India
[80] Niels Bohr Institute, University of Copenhagen, Copenhagen, Denmark
[81] Nikhef, National Institute for Subatomic Physics, Amsterdam, The Netherlands
[82] Nuclear Physics Group, STFC Daresbury Laboratory, Daresbury, UK
[83] Nuclear Physics Institute, Academy of Sciences of the Czech Republic, Řež u Prahy, Czech Republic
[84] Oak Ridge National Laboratory, Oak Ridge, Tennessee, USA
[85] Petersburg Nuclear Physics Institute, Gatchina, Russia
[86] Physics Department, Creighton University, Omaha, NE, USA
[87] Physics Department, Panjab University, Chandigarh, India
[88] Physics Department, University of Athens, Athens, Greece
[89] Physics Department, University of Cape Town, Cape Town, South Africa
[90] Physics Department, University of Jammu, Jammu, India
[91] Physics Department, University of Rajasthan, Jaipur, India
[92] Physik Department, Technische Universität München, Munich, Germany
[93] Physikalisches Institut, Ruprecht-Karls-Universität Heidelberg, Heidelberg, Germany
[94] Politecnico di Torino, Turin, Italy
[95] Purdue University, West Lafayette, IN, USA
[96] Pusan National University, Pusan, South Korea
[97] Research Division and ExtreMe Matter Institute EMMI, GSI Helmholtzzentrum für Schwerionenforschung, Darmstadt, Germany
[98] Rudjer Bošković Institute, Zagreb, Croatia
[99] Russian Federal Nuclear Center (VNIIEF), Sarov, Russia
[100] Russian Research Centre Kurchatov Institute, Moscow, Russia
[101] Saha Institute of Nuclear Physics, Kolkata, India
[102] School of Physics and Astronomy, University of Birmingham, Birmingham, UK
[103] Sección Física, Departamento de Ciencias, Pontificia Universidad Católica del Perú, Lima, Peru
[104] Sezione INFN, Bari, Italy
[105] Sezione INFN, Bologna, Italy
[106] Sezione INFN, Cagliari, Italy
[107] Sezione INFN, Catania, Italy
[108] Sezione INFN, Padova, Italy
[109] Sezione INFN, Rome, Italy
[110] Sezione INFN, Trieste, Italy
[111] Sezione INFN, Turin, Italy
[112] SSC IHEP of NRC Kurchatov institute, Protvino, Russia
[113] SUBATECH, Ecole des Mines de Nantes, Université de Nantes, CNRS-IN2P3, Nantes, France
[114] Suranaree University of Technology, Nakhon Ratchasima, Thailand
[115] Technical University of Split FESB, Split, Croatia
[116] The Henryk Niewodniczanski Institute of Nuclear Physics, Polish Academy of Sciences, Cracow, Poland
[117] Physics Department, The University of Texas at Austin, Austin, TX, USA
[118] Universidad Autónoma de Sinaloa, Culiacán, Mexico
[119] Universidade de São Paulo (USP), São Paulo, Brazil
[120] Universidade Estadual de Campinas (UNICAMP), Campinas, Brazil
[121] University of Houston, Houston, TX, USA
[122] University of Jyväskylä, Jyväskylä, Finland
[123] University of Liverpool, Liverpool, UK
[124] University of Tennessee, Knoxville, TN, USA
[125] University of the Witwatersrand, Johannesburg, South Africa
[126] University of Tokyo, Tokyo, Japan
[127] University of Tsukuba, Tsukuba, Japan
[128] University of Zagreb, Zagreb, Croatia
[129] Université de Lyon, Université Lyon 1, CNRS/IN2P3, IPN-Lyon, Villeurbanne, France

[130] V. Fock Institute for Physics, St. Petersburg State University, St. Petersburg, Russia
[131] Variable Energy Cyclotron Centre, Kolkata, India
[132] Vinča Institute of Nuclear Sciences, Belgrade, Serbia
[133] Warsaw University of Technology, Warsaw, Poland
[134] Wayne State University, Detroit, MI, USA
[135] Wigner Research Centre for Physics, Hungarian Academy of Sciences, Budapest, Hungary
[136] Yale University, New Haven, CT, USA
[137] Yonsei University, Seoul, South Korea
[138] Zentrum für Technologietransfer und Telekommunikation (ZTT), Fachhochschule Worms, Worms, Germany

[a] Deceased
[b] Also at: University of Kansas, Lawrence, Kansas, USA